The changing CO_2 sink in the western Arctic Ocean from 1994 to 2019

Zhangxian Ouyang[1], Yun Li[1], Di Qi[2,3], Wenli Zhong[4], Akihiko Murata[5,6], Shigeto Nishino[6],

Yingxu Wu[2,3], Meibing Jin[7,8], David Kirchman[1], Liqi Chen[3], Wei-Jun Cai[1]*

[1] School of Marine Science and Policy, University of Delaware, Newark, Delaware, USA

[2] Polar and Marine Research Institute, College of Harbor and Coastal Engineering, Jimei

University, Xiamen, China

[3] Key Laboratory of Global Change and Marine-Atmospheric Chemistry of Ministry of Natural

Resources (MNR), Third Institute of Oceanography, Xiamen, China

[4] Key Laboratory of Physical Oceanography, Ocean University of China, Qingdao, China

[5] Global Ocean Observation Research Center, Research Institute for Global Change (RIGC),

Japan Agency for Marine-Earth Science and Technology (JAMSTEC), Yokosuka, Japan

[6] Institute of Arctic Climate and Environment Research, Research Institute for Global Change

(RIGC), Japan Agency for Marine-Earth Science and Technology (JAMSTEC), Yokosuka,

Japan

[7] School of Marine Sciences, Nanjing University of Information Science and Technology,

Nanjing, China

[8] International Arctic Research Center, University of Alaska, Fairbanks, USA

*Corresponding author, email: wcai@udel.edu

Abstract:

The Arctic Ocean has turned from a perennial ice-covered ocean into a seasonally ice-free ocean in recent decades. Such a shift in the air-ice-sea interface has resulted in substantial changes in the Arctic carbon cycle and related biogeochemical processes. To quantitatively evaluate how the oceanic CO_2 sink responds to rapid sea ice loss and to provide a mechanistic explanation, here we examined the air-sea CO_2 flux and the regional CO_2 sink in the western Arctic Ocean from 1994 to 2019 by two complementary approaches: observation-based estimation and a data-driven box model evaluation. The pCO_2 observations and model results showed that summer CO_2 uptake significantly increased by about 1.4 ± 0.6 Tg C decade^{-1} in the Chukchi Sea, primarily due to a longer ice-free period, a larger open area, and an increased primary production. However, no statistically significant increase in CO_2 sink was found in the Canada Basin and the Beaufort Sea based on both observations and modeled results. The reduced sea ice coverage in summer in the Canada Basin and the enhanced wind speed in the Beaufort Sea potentially promoted CO_2 uptake, which was, however, counteracted by a rapidly decreased air-sea pCO_2 gradient therein. Therefore, the current and future Arctic Ocean CO_2 uptake trends cannot be sufficiently reflected by the air-sea pCO_2 gradient alone because of the sea ice variations and other environmental factors.

Key Points

- Both observations and model results conclude that summertime CO_2 sink increased significantly by 1.4 ± 0.6 Tg C decade-1 in the Chukchi Sea.
- Model exercises suggest that increased CO_2 sink in the Chukchi Sea is driven by the reduced sea ice and increased primary production.
- Both observations and model results suggest no significant trend of CO_2 sink in the Beaufort Sea and the Canada Basin between 1994 and 2019.

1. Introduction

The Arctic Ocean was predicted to be an important sink for CO_2 as colder water tends to absorb more atmospheric CO_2 compared to temperate and tropical waters (Bates et al., 2006; Bates and Mathis, 2009), but this CO_2 uptake potential has been questioned by more recent observations (Cai et al., 2010; Else et al. 2013). Accelerated sea ice loss has turned the Arctic Ocean from a perennially ice-covered ocean to a seasonally ice-free ocean, resulting in substantial changes in its carbon cycle and related biogeochemical processes. On one hand, increasing freshwater from ice meltwater and river runoff strengthens the upper ocean stratification (Miller et al., 2019; Ahmed et al., 2020), which suppresses the nutrient supply from deep water and hence surface primary production and the resultant CO_2 uptake (Lewis et al., 2020; Randelhoff et al., 2020). The increased freshwater and river runoff could also mobilize additional carbon and nutrients, further affecting Arctic Ocean primary production and air-sea CO_2 flux (Terhaar et al., 2019). On the other hand, earlier onset of ice melt in the Bering Strait, a gateway to the western Arctic Ocean, allows increased transport of the nutrient-rich Pacific Water into the Arctic Ocean, while earlier ice melt on the Arctic shelves and inside the basins also results in a larger ice-free open area and a longer growing season, both lead to a higher primary production and may substantially influence the CO_2 sink and source status (Arrigo et al., 2010; Zheng et al., 2021a). Other complexities and uncertainties are added by an increase in wind speed and storm events (Mathis et al., 2012; Hauri et al., 2013; Fransson et al., 2017), which greatly affects air-sea gas exchange across the air-ice-sea interface. Thus, it is challenging to quantitatively assess how CO_2 sink changes with loss of sea ice.

The western Arctic Ocean has undergone dramatic climate-driven ice loss and substantial alterations in the seasonal biogeochemical dynamics in recent decades. The western Arctic Ocean consists of the inflow shelf, the Chukchi Sea, which is directly impacted by the nutrient-rich Pacific Ocean Water (Woodgate et al., 2012; Woodgate 2018), the interior shelf, the Beaufort Sea, which is narrow and influenced by the Mackenzie River, and the oligotrophic Canada Basin, which is greatly influenced by the nutrient-poor Beaufort gyre and sea ice meltwater (Ardyna and Arrigo, 2020). The two most contrasting regions, the Chukchi Sea shelf and Canada Basin, have shown quite different responses to climate-related drivers. Specifically, net primary production (NPP) increased by ~96% over 1998-2018 on the Chukchi Sea shelf

(Lewis et al., 2020), while NPP was consistently low over the same time span in the Canada Basin (Ji et al., 2019; Lewis et al., 2020). Additionally, summer sea surface pCO_2 increased at twice the rate of atmospheric CO_2 in the oligotrophic Canada Basin from 1994 to 2017, whereas no significant pCO_2 increase was found on the nutrient-rich Chukchi Sea shelf (Ouyang et al., 2020). Ouyang et al. (2020) further suggested that if these trends of pCO_2 continue, the Canada Basin will not be as large a CO_2 sink as previously estimated (Bates et al., 2006; Bates and Mathis, 2009), and the CO_2 sink on the Chukchi Sea shelf will increase due to the atmospheric CO_2 increase. However, the interannual change in the CO_2 sink of the western Arctic is poorly known. Only a few studies have examined the interannual variation in CO_2 flux and carbon sink, and uncertainties remain large (Arrigo et al., 2010; Yasunaka et al., 2016 &2018; Manizza et al., 2019).

Early attempts to quantify the CO_2 flux and sink in the western Arctic Ocean were largely based on snapshots of a single cruise (Murata and Takizawa, 2003; Bates et al., 2006; Bates and Mathis, 2009; Cai et al., 2014), which likely overestimated or underestimated the carbon sink when instantaneous CO_2 fluxes were scaled to the entire region. With a more extensive pCO_2 dataset collected over 2003-2014, Evans et al., (2015) examined the monthly climatology of air-sea pCO_2 gradients (ΔpCO_2) and CO_2 fluxes for the Chukchi and Beaufort coastal seas. However, this approach still suffered from a sparsity of pCO_2 data, especially for winter months and high latitudes which were covered by sea ice for most of the time. To increase data coverage in both time and space, different approaches have been explored and applied to better estimate the Arctic Ocean CO_2 budget. Arrigo et al., (2010) reconstructed the pCO_2 field in the Arctic Ocean by combining in situ data and remote sensing techniques. Although this technique can provide a pCO_2 map with a very high resolution in time (daily-based), the limitation is that reconstructed pCO_2 only covers spring to fall when satellite data are available. Recently, a two-step neural network method was developed and successfully used for estimating the global ocean carbon budget (Landschützer et al., 2013, 2014, 2016; Laruelle et al., 2017). However, its performance deteriorates in the Arctic coastal seas and the higher latitudes (Laruelle et al., 2017; Roobaert et al., 2019) because of insufficient observations for training the model (Gloege et al., 2020). Also, due to the unevenly observed sea surface pCO_2 in seasons (much more observations in summer and fall than in winter and spring), the performance of neural network method and

data coverage becomes inadequate in winter and spring. Only a few attempts have been made with a coupled physical and biogeochemical model to fill the gaps in the data and to examine temporal and spatial variability of the CO_2 sink (Manizza et al., 2013 & 2019; Zheng et al., 2021b).

To resolve the spatial and temporal variability in air-sea CO_2 flux and to determine how the carbon sink and source change in response to multiple sea ice-related changes, we quantified the air-sea CO_2 fluxes and carbon sink for the western Arctic Ocean from 1994 to 2019. We compiled an extensive dataset of sea surface pCO_2 from several international databases, which extends the assessment to 2019. However, increasing the number of pCO_2 observations still does not fully resolve inadequacies in seasonal and regional coverage, which makes it difficult to assess whether there are any trends in CO_2 fluxes among different regions. To fill these data and knowledge gaps, we used a data-driven box model to reconstruct the daily pCO_2 maps for the western Arctic Ocean from 1994 to 2019. With the model results, we can further disentangle and identify the effects of sea ice, wind speed, and air-sea gradient of pCO_2 on the seasonal and interannual variabilities of CO_2 flux and carbon sink.

2. Methods

2.1. Study Area

The western Arctic Ocean covers the areas between 65°N to 85°N and 125°W to 180°W. According to characteristics of hydrography, topography, ocean circulation, and sea ice condition, we divided the study area into three biogeochemical provinces: (1) the nutrient-rich Chukchi Shelf (CS), which sometimes is further divided into the southern Chukchi Shelf (sCS, 65°N–69°N) and the northern Chukchi Shelf (nCS, >69°N) due to its high spatial heterogeneity; (2) the oligotrophic Canada Basin (CB, <85°N), separated from the Chukchi Shelf mainly along the shelf breaks (~250 m isobaths); (3) the coastal Beaufort Sea (BS), separated from the Chukchi Sea and Canada Basin along 152°W and 72°N, respectively. The highest-latitude area of Makarov Basin with perennial ice cover (>85°N) is not included in the present study (Fig. 1).

2.2. Observation-based CO_2 flux calculation

2.2.1. Data Sets and processing

Underway sea surface pCO₂ data. To examine decadal changes in CO_2 flux in the western Arctic Ocean, we first synthesized a dataset of pCO₂ measurements via multiple international databases (Supplementary Table 1), including Surface Ocean CO_2 Atlas (SOCAT v2020, http://www.socat.info; Bakker et al., 2016), Japan Agency for Marine-Earth Science and Technology (JAMSTEC) data site, DARWIN (http://www.godac.jamstec.go.jp/darwin/e), USGS database (https://pubs.er.usgs.gov), NSF Arctic Data Center (https://arcticdata.io), and Chinese National Arctic and Antarctic Data Center (http://www.chinare.org.cn). This extensive dataset contains more than 513,000 sea surface pCO₂ ($p\mathrm{CO}_2^{\mathrm{sea}}$) data points and associated sea surface temperature (SST) and sea surface salinity (SSS) data. All data are archived in publicly accessible databases (Supplementary Table 1).

For consistency, we chose to report and analyze all the data as pCO₂. Thus, the reported CO_2 fugacity (fCO₂) from some programs (Supplementary Table S1) were converted to pCO₂ at SST using 'seacarb' package in R (Gattuso et al., 2018). Note that the difference between pCO₂ and fCO₂ conversion is less than the measurement precision of ± 2 μatm. Thus, the error induced by conversion is negligible. In particular, the air-sea gradient ΔpCO₂ and ΔfCO₂ are essentially the same.

Discrete sea surface pCO₂ data. To expand the data coverage in both time and space in the analysis, we added pCO₂ data calculated from dissolved inorganic carbon (DIC) and total alkalinity (TAlk) data based on discrete samples taken in the surface mixed layer (5m< depth <20 m). The discrete DIC and TAlk data were obtained from the Global Data Analysis Project version 2 database 2019 (GLODAP v2.2019). The pCO₂ was calculated by the 'seacarb' package in R (Gattuso et al., 2018) with carbonate dissociation constants of Millero et al., (2006) recommended by Evans et al., (2015). The uncertainty of pCO₂ values computed from TAlk and DIC is about ± 13 μatm with a mean systematic difference from the measured pCO₂ of -0.7 μatm (Woosley et al., 2017).

Air pCO₂. The $p\mathrm{CO}_2^{\mathrm{air}}$ was calculated from monthly average atmospheric CO_2 concentrations in dry air (xCO₂) measured at Point Barrow, Alaska (https://www.esrl.noaa.gov/gmd/dv/data/index.php?parameter_name=Carbon%2BDioxide&frequency=Monthly%2BAverages&site=BRW). Then xCO₂ was corrected to pCO₂ for water vapor pressure:

$$pCO_2^{air}{}_{(daily)} = xCO_{2(monthly)} \cdot (Psl_{(daily)} - Pw_{(daily)}) \qquad (2)$$

where Psl is sea level pressure and Pw is water vapor pressure. Daily Psl data were obtained from a satellite reanalysis product (NCEP-DOE Reanalysis 2, https://www.esrl.noaa.gov/psd/data/gridded/data.ncep.reanalysis2.html) with a resolution of 2.5° × 2.5°. Daily Pw data were calculated from Psl and SST (Buck, 1981). Considering the uncertainties from sea level pressure data and the water vapor saturation pressure, the overall uncertainty of air pCO_2 is about 0.5 μatm (Yasunaka et al., 2016 & 2018).

Wind speed second moments. The second moment of wind speed at 10 m height $<U_{10}^2>$ was obtained from the NCEP-DOE Reanalysis 2 data with a spatial resolution of 1.8750° in longitude and 1.9041° in latitude. (https://www.esrl.noaa.gov/psd/data/gridded/data.ncep.reanalysis2.html). For each day, the 6-hourly wind speed squared was calculated and then averaged into a daily mean and subsequently into a monthly mean value according to the temporal resolution of CO_2 flux calculation.

Sea ice concentration. Daily sea ice concentration (ice%) was obtained from the Scanning Multichannel Microwave Radiometer (SMMR) on the Nimbus-7 satellite and the Special Sensor Microwave/Imager (SSM/I) sensors on the Defense Meteorological Satellite Program's (DMSP)-F8, -F11, and -F13 satellites with a resolution of 25 km × 25 km (Comiso, 2017).

2.2.2.   Monthly CO_2 flux calculation

In general, our method follows Laruelle et al., (2014) and Evans et al., (2015) with a few modifications. Figure 2 shows the scheme of observation-based CO_2 flux calculation. The synthesized pCO_2 datasets associated with SST and SSS were averaged into 1° latitude × 1° longitude grids for each day, then into each month in a particular year. Accordingly, all other parameters of pCO_2^{air}, $<U_{10}^2>$, and ice% were re-gridded into 1° latitude × 1° longitude grid and averaged into a monthly mean to match gridded pCO_2^{sea}. The monthly air-sea CO_2 flux (F_{CO2}, unit: mmol C m^{-2} d^{-1}) for each 1° latitude × 1° longitude grid was calculated following,

$$F_{CO2} = K_s \cdot k_{CO2} \cdot (pCO_2^{sea} - pCO_2^{air}) \qquad (3)$$

where K_s is the solubility of CO_2 (mol m^{-3} atm^{-1}), and k_{CO2} is the CO_2 gas transfer velocity (m d^{-1}). The K_s was calculated using underway SST and SSS (Weiss, 1974). The value of k_{CO2} is estimated from the parameterization of Wanninkhof (2014), depending on the second moment of wind speed at 10 m height above the sea surface, $<U_{10}^2>$ (m^2/s^2):

$$k_{CO2} = 0.251 \cdot <U_{10}^2> \cdot (Sc/660)^{-0.5} \tag{4}$$

Laruelle et al., (2014) and Evans et al., (2015) first corrected CO_2 flux for ice cover by applying a linear ice correction (Butterworth and Miller, 2016; Prytherch et al., 2017) in each grid, which had sea surface pCO_2 data (Equation 5), and then averaged all CO_2 fluxes into a monthly regional mean by considering weighting of the area in each grid (Equation 6; Fig. 2).

$$F_{CO2\ (ice\text{-}corrected)(i)} = F_{CO2(i)} \times (1\text{-}ice\%_{(i)}) \tag{5}$$

$$F_{CO2(area\text{-}weighted)} = \sum_{i=1}^{n}(FCO_{2(i)} \times (1 - ice\%_{(i)}) \times A_i) / \sum_{i=1}^{n} A_i \tag{6}$$

where i represents the ith grid with pCO_2 observations present and A is the area of the corresponding grid. This upscaling method was designed for the western Arctic coastal ocean and works well for these regions where sea ice concentration is relatively lower or uniform and data coverage of sea surface pCO_2 observations is relatively higher. However, only correcting ice% in the grids where pCO_2 observations exist may underestimate the impact of sea ice on CO_2 flux calculation in a region with large sea ice gradients (i.e., Canada Basin) when a regional mean of CO_2 flux is upscaled to the entire region. For example, most sea surface pCO_2 observations were concentrated in the southern Canada Basin, thus, it may overweight the observed fluxes in the southern grids with a much lower ice coverage or no ice when we extrapolate the observed regional mean to the entire Canada Basin. Therefore, we modified the calculation of regional CO_2 flux by changing the sequence of the CO_2 flux calculation and correction of sea ice concentration (red arrows in Fig. 2), an approach we believe will better account for the impact of sea ice (see more discussion in supplementary information). Briefly, we first calculated an area-weighted monthly CO_2 flux (without ice correction) from all gridded CO_2 flux for a given subregion (equation 7; Step 1 in Fig. 2), and assumed that this regional

monthly CO_2 flux can largely represent the potential magnitude in CO_2 flux for the entire biogeochemical province in the respective month.

$$F_{CO2(area\text{-}weighted)} = \sum_{i=1}^{n}(F_{CO2(without\,ice\,correction)\,(i)} \times A_i) / \sum_{i=1}^{n} A_i \qquad (7)$$

Then, we corrected CO_2 flux for sea ice concentration (ice%) presented in that month for each grid as follows (equation 8; Step 2 in Fig. 2),

$$F_{CO2(corrected)i} = F_{CO2(area\text{-}weighted)} \times (1\text{-}ice\%_{(i)}) \qquad (8)$$

In this way, we can extrapolate a regional monthly mean of CO_2 flux to all grids, and then correct for ice cover in every grid to generate a CO_2 flux map. Note that because the satellite data are unable to resolve fine-scale ice structure (i.e., cracks and leads) that allows air-sea gas exchange, we adopted the technique used by Takahashi et al. (2009) that assumes ice% always equals 90% to allow weak gas exchange for the grids where satellite ice% is greater than 90%. Finally, we can compute monthly area-weighted CO_2 flux for a particular subregion using CO_2 fluxes values in all grids in that subregion following equation (6). Although not all months have pCO_2 observations, we assumed that the CO_2 flux in a given month without any observation is similar to the climatological monthly mean in that month. Therefore, we first filled the data gap with climatological monthly means within each subregion for the periods of 1994-2006 and 2007-2019 and then filled the remaining gaps across all the subregions (Supplementary Tables S6-9).

2.3. Model-based CO_2 flux calculation

Although we attempted to extend monthly mean CO_2 fluxes derived from limited data points to the entire subregions, this upscaling method alone was deemed to be insufficient. For instance, few observations were made in winter and spring. Although the CO_2 flux is expected to be near zero in the ice-covered winter, it could be substantial during the early ice-free season in spring and ice formation period in the fall (Juranek et al., 2019). It is thus hard to assess the year-round CO_2 flux or interannual variations. Here, we employed a data-driven box model to reproduce pCO_2 time series and spatial distribution from 1994 to 2019 and to examine the complex

seasonal and interannual dynamics of CO_2 flux and CO_2 uptake. Despite its simplicity, the model simulation allows us to increase temporal resolution from monthly to daily, which greatly facilitates understanding short-term CO_2 flux fluctuations associated with rapid changes in sea ice. Finally, we used this modeled pCO_2 dataset to assess the possible trends of CO_2 flux and carbon sink in the western Arctic Ocean.

2.3.1. Data sources.

The daily sea surface temperature (SST) data were obtained from a Group for High Resolution Sea Surface Temperature (GHRSST) Level 4 sea surface temperature (SST) analysis (https://podaac-opendap.jpl.nasa.gov/opendap/allData/ghrsst/data/GDS2/L4/GLOB/CMC/CMC0.2deg/v2/). We compared the SST and observed underway SST within a given grid on the same day. The r^2 are 0.73, 0.60, 0.84 and the RMSE are 1.7 .0.9 and 1.3 ℃ for the Beaufort Sea, the Canada Basin, and the Chukchi Sea, respectively (Fig. S1). Although SST affects several calculations in pCO_2 simulation and CO_2 flux estimation, the uncertainty induced by SST is much smaller compared to uncertainties of parameterization of gas exchange. The uncertainty of SST is propagated into ΔpCO_2 and considered in the final CO_2 flux calculation (See section 2.5).

The daily sea surface salinity (SSS) and mixed layer depth (MLD) data were obtained from global ocean ensemble physics reanalysis product (https://resources.marine.copernicus.eu/?option=com_csw&view=details&product_id=GLOBAL_REANALYSIS_PHY_001_031). Prior to directly using SSS product in our model, we compared the modeled and observed SSS within a given grid on the same day. We noticed that although the product assimilated observed salinity profiles, they are limited in space and time, especially lack automated observations (such as ITP) before 2000. This SSS product also tended to have a much lower decline rate in SSS during 1994-2019 and a higher surface salinity (by 0.5~2 psu) for summer months (July to October) after 2000. Therefore, we adjusted SSS by first removing the trend of residuals and then reduced apparent systematic bias based on the mean of residuals in a given month for each subregion. After adjustment, the root mean square error (RMSE) of residuals were 2.5, 1.0, and 1.2 psu in the Chukchi Sea, the Beaufort Sea, and the Canada Basin, respectively (Supplementary Fig. S1).

The data sources of the daily second moment of wind speed ($<U_{10}^2>$), sea ice concentration (ice%), and the reconstructed air pCO_2 were described in section 2.2.1. All datasets used in the model simulation were re-gridded from their original spatial resolution to a $1° \times 1°$ grid.

2.3.2.   Model setting and simulation step.

Estimate of total alkalinity (TAlk). Total alkalinity in surface water was calculated from SSS. The relationship between TAlk and SSS was determined by using the discrete samples obtained from the Global Data Analysis Project version 2 database (Olsen et al., 2020). To minimize the potential error induced by the near-surface meltwater (Miller et al., 2019; Ahmed et al., 2020), and to better establish the relationships between TAlk and SSS reflected by underway water (intake is ~7 m below the waterline), we removed discrete sample collected in the shallow freshwater layer (<5 m) before we did linear regression for TAlk vs salinity. In addition, we noticed that the relationships varied with months and regions due to seasonal river runoff input and the sea ice melt and formation cycle. Therefore, we established the relationships between SSS and TAlk for each month and separately for the Chukchi Shelf, the Beaufort Sea, and the Canada Basin (Supplementary Table. S2). For the months without any observation (almost always the winter months), we linearly interpolated the slope and intercept of the relationship using the adjacent months' values assuming that the seasonal evolution of SSS and TAlk is relatively slow and smooth.

Net Community Production (NCP). The NCP estimates in the Chukchi Shelf and Canada Basin reported in previous studies are summarized in Supplementary Table S3. As primary production is patchy and widely variable on the shelf and in coastal regions on the interannual time scale, it is very difficult to set values for each month or find the best value suitable for the entire region. However, we noticed some general patterns for seasonal variation in NCPs in all three subregions. All across the western Arctic Ocean — in the shelf, slope, and southern basin areas — the growing season starts in May–June. The NCP peaks appear in June-July, possibly shifting earlier in the southern Chukchi Shelf and later in the northern Canada Basin. However, due to different nutrient supply mechanisms (Ouyang et al. 2020; Mathieu and Arrigo, 2020), the evolution of NCPs deviates from each other in the three subregions as the seasons proceed. The Chukchi Shelf benefits from sustained nutrient supply from Pacific Water, which supports a high

NPP lasting from summer to fall. The coastal Beaufort Sea nutrient supply for the surface mixed layer is mainly from river discharge, upwelling, and local water mixing, which can create some potential biological hotspots. However, it is likely to be only locally important because the nutrients are contained and consumed within near-coastal regions (Tremblay et al., 2014; Ardyna et al., 2017). In contrast, nutrient sources and supplies are limited in the Canada Basin, only being from ice-trapped brine and the remaining in the mixed layer from the previous winter. Furthermore, summer stratification strengthens its oligotrophic characteristics (Ji et al., 2019; Mathieu and Arrigo, 2020). Interestingly, a recent study further found that NCP in the Canada Basin is closely associated with ice melting stages (Ouyang et al., 2021). Therefore, instead of using monthly averaged NCP, we incorporated NCP estimation based on the relationship between ice concentration and NCP into our model. Briefly, NCP (5.6 ± 2.0 mmol C m^{-2} d^{-1}) was relatively high during the actively melting period (ice% from 30% to 50%), whereas NCP (1-2 mmol C m^{-2} d^{-1}) was lower in the pre-melt (ice% >80%) and post-melt period (ice% < 15%) (Supplementary Fig. S2). This relationship was established by examining the histories of wind and ice in a given location combined with the underway measurement of $\Delta(O_2/Ar)$ (Ouyang et al., 2021).

A recent study reported that Chl a concentration and net primary production (NPP) increased by 26% and 96%, respectively, on the Chukchi Shelf from 1998 to 2018 (Lewis et al. 2020). We quantified NCP increase rates from NPP by multiplying f-ratios (NCP=NPP×f), which are 0.3 and 0.2 for the southern and northern Chukchi Sea, respectively (Codispoti et al., 2013). Thus, we applied an increase of NCP by 29% (96%× 0.3) and 19% (96%× 0.2) from 1994 to 2019 in the southern and northern Chukchi Seas, respectively, in our model. Meanwhile, we also performed a sensitivity test without NCP increase to test how NCP change affects CO_2 sink in the Chukchi Sea. In contrast, the NCPs in the Canada Basin and the Beaufort Sea were much lower than that on the Chukchi Shelf and no significant trend was found in the Canada Basin and only a slight increase (less than 10%) was found in the Beaufort Sea (Lewis et al. 2020). Thus, we set a constant seasonal cycle of NCP over the simulation period in these two regions. The NCPs used in our model are presented in Supplementary Table S4.

Simulation step. The two goals of this simple model excise are to fill the data coverage gaps in both temporal and spatial and to evaluate the CO_2 flux and CO_2 sink trends in the western Arctic Ocean. The model resolution is 1 day in time and $1° \times 1°$ grid in space. The initial sea surface pCO_2 was set as 340 μatm according to atmospheric pCO_2 in 1994 for all grids on the first day of simulation. Note that our box model is not sensitive to the initial input of sea surface pCO_2 since we performed a 5-year baseline run before the simulation of 1994-2019. In this baseline run, we repeatedly using the datasets of 1994 to run a simulation for 5 years to constrain the mean state of carbonate parameters mediated by physical and atmospheric forcings. We used the data on the last day in the baseline run as initial input for the following simulation of 1994 -2019. In this way, we can minimize the biases induced by initial settings. Then, the outputs of 1994 - 2019 were analyzed.

For each simulation step in each grid, sea surface pCO_2 was calculated from TA and DIC at the corresponding step using the 'seacarb' package in R (Gattuso et al., 2018). The daily change in DIC inventory in the surface mixed layer was calculated as follows:

$$\Delta DIC_t = \Delta DIC_{(diluted)t} - (FCO_{2t} + NCP_t - E_t) \times \Delta t / (MLD_t \times \rho) \qquad (9)$$

where $\Delta DIC_{(diluted)t}$, FCO_{2t}, and NCP_t, indicate the changes in DIC inventory in the mixed layer induced by meltwater dilution, CO_2 air-sea flux, and net community production at simulation time step t, respectively. The surface seawater density, ρ, is calculated using SST and SSS. The calculation of FCO_2 term was similar to equation (3) with daily ice% correction (equation 8). We computed the change in DIC by dilution ($\Delta DIC_{(diluted)t}$) by simplifying the ice melt dilution or ice formation processes in the simulation and assuming that the ratio of TA/DIC in the ice is equal to that in the surface seawater. Thus,

$$\Delta DIC_{(diluted)t} = (TA_{t+1} - TA_t) / TA_t \times DIC_t \qquad (10)$$

Due to the limitations of the box model, the physical mixing processes are dependent on the variations of SSS and MLD. Thus, we are not able to resolve vertical or lateral mixing. Therefore, we introduced an adjustable error term (E) to equation (9). This error term accounts

for any other perturbation in DIC inventory, such as respiratory DIC addition, deep water upwelling, local water mixing, and brine rejection. We adjusted the E term for each month and for each subregion to minimize the systematic bias (See more description in section 2.4). DIC at time step $t+1$ was iteratively calculated as follows,

$$DIC_{t+1} = DIC_t + \Delta DIC_t \qquad (11)$$

With the new DIC and TA for the next simulation step, a new pCO_2 was calculated, and this simulation process repeats until the last day. In short, this data-driven model provides a daily pCO_2 map with $1° \times 1°$ spatial resolution over the entire western Arctic Ocean from 1994 to 2019, driven by data and the associated processes and mechanisms.

2.4. Model validation

To evaluate the performance of our box model, we compared simulated pCO_2 with the synthesized pCO_2 on the same day at the given grid. Over the entire western Arctic Ocean, the mean of differences between simulated and observed pCO_2 is -0.4 µatm and the root mean square error (RMSE) is 50.2 µatm. The model performance varies among the three subregions. More specifically, simulated pCO_2 better fits the observed pCO_2 in the Canada Basin than in the Beaufort and Chukchi Seas. Based on daily resolution results, the RMSEs of the residuals are 31 µatm, 42 µatm, and 63 µatm in the Canada Basin, Beaufort Sea, and Chukchi Sea, respectively (Supplementary Fig. S3). This is likely because the model could not capture some high-frequency variabilities in the shelf regions including coastal upwelling in the Beaufort Sea and patchy biological production and vertical mixing in the Chukchi Sea. The residuals in all three subregions have a normal or nearly normal distribution and the average biases are less than ± 5 µatm (Supplementary Fig. S3). When we average daily pCO_2 into a monthly mean to do a further comparison, the RMSEs of the residuals become smaller (26 µatm, 38 µatm and 62 µatm in the Canada Basin, Beaufort Sea, and Chukchi Sea, respectively), which are comparable to the results of the biogeochemical model in the Chukchi Sea (Zheng et al., 2021b), as well as the results of neural network interpolation approaches which are also based on a monthly time resolution (Laruelle et al. 2017; Yasunaka et al. 2018) over the entire western Arctic Ocean.

While the comparison of residuals and RMSEs allows us to quantitatively assess the performance of our model, it does not provide sufficient information about the validity of the reconstruction of complex seasonality of $p\text{CO}_2$. To check this capability, we further examined the average residual and RMSE for each month in a particular subregion. We found that, in the absence of vertical and lateral mixing terms in the box model, air-sea CO_2 exchange term alone does not adequately replenish DIC pool in the mixed layer in the fall and winter in the Chukchi Sea and Beaufort Sea. To reduce this systematic error, we constrain the average residual of $p\text{CO}_2$ in each month to ±10 µatm by adjusting the error term, E in equation (9) (Supplementary Table S5). Through trial-and-error processes, we found that it is not necessary to have an error term in the Beaufort Sea and the northern Chukchi Sea from May to October to achieve the criteria if we adopted NCPs from the higher-end of the reported range for the early growing season and from the lower end of the reported range for the late growing season (Table S3-S5). That said, the net biological CO_2 removal is more efficient in late spring and early summer compared to it in the late summer and fall. One possible reason is that stronger wind in the late season may induce strong upwelling and vertical mixing, which releases the early season's respiration products back to the surface mixed layer. Although the ecosystem still could be autotrophic with high NPP during the late growing season, the NCP of the entire ecosystem becomes much weaker. However, a negative E is needed for some months through late summer to fall in the southern Chukchi Sea to achieve the criteria of average bias of ±10 µatm. A negative E indicates an addition of DIC in the mixed layer, which accounts for the Pacific inflow advection of DIC or local mixing with deep water on the shelf. In contrast, there is no apparent seasonal discrepancy between modeled and observed $p\text{CO}_2$ in the Beaufort Sea and Canada Basin, indicating that DIC perturbation due to mixing in this region is minimum due to a strong summer stratification. Thus, we set the E term to 0 for both the Beaufort Sea and Canada Basin (Supplementary Table S5). For winter and early spring, a small negative E (up to -2 µmol kg^{-1} day^{-1}) is set to account for possible net respiration and winter ventilation in the Chukchi Sea and the Beaufort Sea (Supplementary Table S5; Shadwick et al., 2011). Adding an E-term not only leads to a smaller RMSE, but also better captures $p\text{CO}_2$ seasonality. We checked the simulated climatological monthly mean of $p\text{CO}_2$ against the observed monthly means extracted from the SOCAT dataset (Supplementary Fig. S4). We give the comparisons in 15 grids that represent the typical locations with relatively more abundant observed data. Generally, our simulation captures the seasonality

of pCO_2 throughout spring to fall on the Chukchi Sea shelf and in the Beaufort Sea. Maximum pCO_2 appears in the late spring before the growing season start whereas minimum pCO_2 appears in the early summer. In contrast, the modeled climatological monthly pCO_2 deviated more from the observed seasonality of pCO_2 in the Canada Basin because the climatological monthly means can lump the interannual variations in pCO_2, which primarily depends on the interannual variation in ice conditions (DeGrandpre et al., 2020). From the simulated results, we noticed that the seasonality of pCO_2 changes in both phase and magnitude in the periods before and after the year 2007, in which the western Arctic Ocean experienced a massive sea ice retreat. Since then, multi-year ice was gradually replaced by first-year ice. However, it is very challenging to validate this shift with limited observations.

2.5.   Uncertainty analysis

There are two main uncertainties in estimating the CO_2 flux. The gas exchange velocity parameterization contributes the largest uncertainty source, which is about 20% (Wanninkhof, 2014). Applying an ice correction for gas exchange velocity could further enlarge the uncertainty up to ~40% (Loose et al., 2014; Lovely et al. 2015). The second uncertainty for CO_2 flux comes from analytical errors. The uncertainty for the measurements is about ± 0.5 µatm for air pCO_2 and ± 2 µatm for sea surface pCO_2. Accounting for a few pCO_2 data points calculated from DIC and TA with an uncertainty of ± 5-7 µatm (Chen et al., 2015; Woosley et al., 2017), the total uncertainties for pCO_2 measurements are less than 1% of the long-term mean. Combined with an uncertainty of 5% for sea-ice concentration (Peng et al., 2013) and uncertainties of 20% to 40% for gas exchange velocity parametrization, we estimated the overall uncertainty of the observation-based CO_2 fluxes calculation to be 21% to 42%, following the error propagation equation (i.e. $[0.2^2(or\ 0.4^2) + 0.05^2 + 0.01^2]^{0.5}$).

For the estimates using model pCO_2, additional uncertainty comes from the deviation between simulated pCO_2 and observed pCO_2. As the pCO_2 observations are unevenly distributed in season, we separately assessed the uncertainties of simulated pCO_2 for winter-spring (November to June) and summer-fall (July to October) for each subregion. For winter-spring, the uncertainties of simulated pCO_2 (RMSE) are 16 µatm, 42 µatm, and 77 µatm in the Canada Basin, Beaufort Sea, and Chukchi Sea, respectively, which are about 30%, 76%, 83% of the

long-term average $\Delta p\mathrm{CO_2}$ in winter-spring in the respective subregion. Accordingly, the uncertainties of model-based $\mathrm{CO_2}$ fluxes in winter-spring are 42%, 84%, and 88% in the Canada Basin, Beaufort Sea and Chukchi Sea, respectively, assuming the uncertainties of for gas exchange velocity parametrization is 30% (i.e., $[0.3^2 + 0.05^2 + 0.01^2]^{0.5}$+(uncertainty of simulated $p\mathrm{CO_2}$)^2). For summer-fall, the uncertainties of simulated $p\mathrm{CO_2}$ (RMSE) are 31 µatm, 42 µatm, and 61 µatm in the Canada Basin, Beaufort Sea and Chukchi Sea, respectively, which are about 61%, 82%, and 58% of the long-term average $\Delta p\mathrm{CO_2}$ in summer-fall, resulting in uncertainties of 68%, 88% and 65% in $\mathrm{CO_2}$ fluxes in respective subregions.

3. Results

3.1. Monthly climatology of $\Delta p\mathrm{CO_2}$ and $\mathrm{CO_2}$ flux

With the synthesized $p\mathrm{CO_2}$ dataset, we examined the monthly climatology of the air-sea gradient of $p\mathrm{CO_2}$ (that is $p\mathrm{CO_2^{sea}} - p\mathrm{CO_2^{air}}$) and $\mathrm{CO_2}$ flux over years from 1994 to 2019. Although the $p\mathrm{CO_2}$ observations were unevenly distributed in space and time, we can still clearly see the different patterns in $\Delta p\mathrm{CO_2}$ between winter-spring (November to June) and summer (July to October). A weak positive $\Delta p\mathrm{CO_2}$ (<45 µatm) was sustained from December through April, according to a limited number of observations in the Beaufort Sea (Fig. 3). These results suggest weak $\mathrm{CO_2}$ outgassing (positive flux in Fig. 4) over the western Arctic Ocean during winter-spring. The highest positive $\Delta p\mathrm{CO_2}$ appeared in May and early June in the northern Chukchi Sea and the mouth of Mackenzie River, ranging from 100 to 200 µatm (Fig. 3), which reflected a potential strong carbon source in those areas (Fig. 4). These high positive $\Delta p\mathrm{CO_2}$ values likely reflect the accumulation of $p\mathrm{CO_2}$ produced as a result of the water column and benthic respiration in nearshore waters over the winter and early spring under the ice cover.

The transition of the carbon source-sink status occurred in late May through early June. The areas of positive $\Delta p\mathrm{CO_2}$ reduced as sea ice retreated and more areas with negative $\Delta p\mathrm{CO_2}$ extended from the southern Chukchi Sea to the northern part and from the Beaufort coastal sea into the Canada Basin in the following summer months. Starting in July, the Chukchi Sea turned into the largest $\mathrm{CO_2}$ sink in the western Arctic Ocean as a result of high primary production (Zheng et al., 2021a & 2021b), indicated by the greatest negative $\Delta p\mathrm{CO_2}$ (-150 to -200 µatm). These negative $\Delta p\mathrm{CO_2}$ values can persist through the entire summer to September in the Chukchi

Sea. Interestingly, the strongest CO_2 uptake ($\sim$ -25 mmol C m^{-2} d^{-1}) appears in early October in the northern Chukchi Sea (Fig. 4), although ΔpCO_2 is not as large as it is in early summer. This strong CO_2 sink is likely due to the increased wind speed in the late summer and fall. In contrast, the large negative ΔpCO_2 during the early growing season could not be maintained through the end of summer in both the Beaufort Sea and central Canada Basin (Fig. 3). Instead, ΔpCO_2 gradually reduced in absolute size toward the atmospheric equilibrium, indicating a weakening carbon sink as the seasons progressed (Fig. 4). At a few locations in the southern Canada Basin and Beaufort Sea, ΔpCO_2 can even become positive during extreme warming and wind-driven events and change the region from a CO_2 sink to a CO_2 source. However, this transition lasted only for a few days to weeks, which cannot change the dominant summer-fall carbon sink status of the Canada Basin and Beaufort Sea. Note that the variation in ΔpCO_2 at the higher latitudes in summer was relatively small due to a much less ice melt and less warming and much weaker biological activity. Starting in November as sea ice started to form, ΔpCO_2 might shift from negative to positive again in the Beaufort Sea and Canada Basin, which is likely a result of brine rejection and vertical mixing during ice formation (Shadwick et al., 2011; Else et al., 2012). In addition, a large area of positive ΔpCO_2 and CO_2 flux appeared in the southern Chukchi Sea, which is likely due to benthic respiration, vertical mixing, and the DIC influx from Pacific inflow advection.

3.2 Seasonal and interannual variabilities of regional CO_2 flux

Due to the unique environmental settings in the Arctic Ocean, the direction and magnitude of the CO_2 flux is not only determined by ΔpCO_2 but is also greatly regulated by sea ice. Thus, we reported the area-weighted monthly CO_2 flux for each subregion with three values: (1) CO_2 flux without ice correction, (2) CO_2 flux first adjusted for sea ice concentration (ice%), and then area-extrapolated following the procedure given in Evans et al., (2015), and (3) CO_2 flux first area-extrapolated and then adjusted for ice% following the modified approach in this study (Fig. 5 and Supplementary Tables S6-9). The values of air-sea CO_2 flux without the ice% correction provide an upper bound of CO_2 flux for the future Arctic Ocean, in which sea ice disappears in the summer and is much less in the winter. Furthermore, the difference between CO_2 fluxes with and without ice% correction clearly reflects the suppression of CO_2 gas exchange by sea ice.

After filling in data gaps (see Section 2.2.2), a more complete seasonal cycle of CO_2 flux appeared. For the winter-spring months (November to June), the potential CO_2 efflux was suppressed by ice cover (Fig. 5; Supplementary Fig. S5), resulting in a very weak sea-to-air CO_2 flux ($\sim$ 0.4-1.0 mmol m^{-2} d^{-1}) in all subregions. Because of this reason, the potential large uncertainty in estimating winter-spring pCO_2 due to lack of sufficient observational data likely will not dominate the uncertainties in the annual flux estimation. As larger areas became open water in the subsequent season and the growing season started, the rate of CO_2 uptake from the atmosphere gradually strengthened. The largest influx of CO_2 repeatedly occurred in September and October due to relatively large ΔpCO_2 and the strongest wind during the year (Evans et al., 2015). The long-term means of monthly CO_2 fluxes among summer months can reach up to -7.5, -5.0, and -19.4 mmol m^{-2} d^{-1} in the Beaufort Sea, Canada Basin, and Chukchi Sea, respectively (Fig. 4 and Supplementary Table S6-9). Starting in November, the CO_2 influx may shift to an equilibrium or an outgassing state. Such patterns of seasonal CO_2 flux evolution were generally similar to each other in all subregions, but some new features on a finer scale in the Beaufort Sea have appeared in recent years. For example, an initial strong CO_2 uptake in early summer (July) was rapidly weakened in late summer (August to September), and then strengthened again in October (Supplementary Fig. S5a).

By comparing CO_2 fluxes derived from Evans et al., (2015) with our modified approaches, we found that the difference was relatively small in both the Beaufort Sea and Chukchi Sea (Fig. 5 a and c), in which data coverage is higher and seasonal cycles of ice retreat and advance were relatively stable from year to year. The difference, however, becomes much larger in the Canada Basin (Fig. 5b). For instance, the monthly CO_2 flux estimated by Evans et al. (2015) approach can be up to 5 times higher than the results of our modified approach (Fig. 5b). Methodologically, the relatively higher values by Evans et al. (2015) approach came from overweighting the observed fluxes in the southern Canada Basin, where higher CO_2 fluxes coincide with larger open-water areas. The nonlinear effects between those two factors in the method led to a potential bias in the assessment of regional average. In comparison, our modified approach applied the sea ice correction on a pre-weighted FCO_2, largely reducing the artifacts (see discussion in Supplementary Information). As such, we chose the modified method for the subsequent analysis of seasonal and interannual variability. As the CO_2 uptake in the summer

months (July- October) dominates the annual flux, we used the summer maximum-to-minimum difference and annual summer mean to characterize the seasonal range and interannual variability of air-sea CO_2 flux (Fig. 6). We noticed that the CO_2 flux in a low-ice year tended to be large (e.g., massive melting events in 1998, 2007, 2008, and 2012 were likely to induce larger CO_2 fluxes), while the CO_2 flux in a high-ice year (1994,1996, and 2013) was weak (Fig. 6; Supplementary Fig. S6). By comparing seasonal and interannual variations in CO_2 fluxes, we also found that, for most years, the Canada basin is the region where interannual variations exceed the seasonal variation, whereas the opposite occurred in the Beaufort and Chukchi Seas where seasonal variations are huge (Fig. 6). However, the CO_2 fluxes did not always follow sea ice changes and other climate drivers may play a role.

3.3. Seasonal and interannual variabilities of regional CO_2 sink

To examine the long-term change in total CO_2 sinks under multiple climate drivers, we compared three calculations of the CO_2 sink (Fig. 7). For the first approach, we used the area-weighted monthly means of CO_2 flux to multiply the days of the month and the ocean surface area to compute the total CO_2 sink in a given subregion (followed the methods in Evans et al., 2015). The second one is our modified approach (see Method; Fig. 2). Using the monthly CO_2 flux map corrected for every 1°×1° grid, we calculated the amount of CO_2 uptake or outgassing in each grid and integrated all grids to get the monthly carbon sink for the given subregion (Steps 2-3 in Fig. 2). For the third approach, we used modeled pCO_2 to calculate daily CO_2 flux for each 1°×1° grid, and then summed up the results of all grids into a regional monthly value.

All three subregions showed a similar seasonality in CO_2 sinks, characterized by a near-neutral or a very weak CO_2 source in winter and spring and a much larger CO_2 sink in summer and fall (Fig. 7). CO_2 uptake in July through October contributed 95-99% and 58-93% of the total year-round sink based on observations and modeled results, respectively (Table 1). Similar to the CO_2 flux estimate, the difference in the CO_2 sink between Evans et al., (2015) and our modified approaches was smaller in both the Beaufort Sea and Chukchi Sea (Fig. 7 a and c), while it becomes much larger in the Canada Basin (Fig. 7b). We found that our box model largely captured the seasonal and interannual variations in all three subregions. However, it may not be able to capture the extreme values in a particular month in a particular year, when it involves

large seasonal and interannual variations in river discharge in the Beaufort Sea and extremely strong primary production in the Chukchi Sea (Fig. 7 a and c). Although the modeled results are more likely reflecting a mean state of CO_2 sink mediated by main physical and biogeochemical drivers in each subregion, it is encouraging that the modeled results matched well with the results of our modified observation-based approach, especially in the Canada Basin. Therefore, we will focus on the result of our modified approach and modeled results in the following discussion.

4. Discussion

4.1. Long-term trend of the CO_2 sink

Although our analysis showed that the CO_2 sink varied from year to year, the estimated long-term means of CO_2 sinks agree well with recent studies (Arrigo et al., 2010; Evans et al., 2015; Manizza et al., 2019; Zheng et al., 2021b; Table 2), but at the lower end of earlier estimates (Bates et al., 2006; Bates and Mathis, 2009; Table 2). The means of the CO_2 sink based on observations taken over several years were -1.9±0.6, -4.4±1.3 and -12.1±3.6 Tg C yr^{-1} in the Beaufort Sea, Canada Basin, and Chukchi Sea, respectively (Table 1). The modeled results showed similar mean values but with a larger uncertainty: -1.5±1.2, -6.6±4.0 and -14.4±8.6 Tg C yr^{-1} in the Beaufort Sea, Canada Basin, and Chukchi Sea, respectively. Compared with estimates in Evans et al., (2015), our estimated CO_2 sink in the Beaufort Sea agrees with theirs, but our estimated CO_2 sink in the Chukchi Sea (-12.1 Tg C yr^{-1}) was much higher than their estimate of -4.4 Tg C yr^{-1}. As estimates of CO_2 flux agree well with each other, this is mostly due to the difference between the areas of Chukchi Sea used in the sink estimates (2.9×10^{11} m^2 in Evans et al., (2015) and 6.6×10^{11} m^2 in this study). Correcting for this difference in areas brings the two estimates much more in line. Their carbon sink becomes ~-10.0 Tg C yr^{-1}, which is comparable to our result and the results of -9.0±1.1 Tg C yr^{-1} in Arrigo et al., (2010), -13.3±2.5 Tg C yr^{-1} in Manizza et al., (2019), and -9.2 ± 1.1 Tg C yr^{-1} in Zheng et al., 2021b (Table 2). Combining all three subregions together, the mean carbon sink for the entire western Arctic Ocean was -18.4±5.5 Tg C yr^{-1} based on observation and -22.5±13.8 Tg C yr^{-1} from our model (Table 2). These estimated CO_2 sinks agreed well with the numerical model result of -17.6±5.0 Tg C yr^{-1} (Manizza et al., 2019) and the remotely sensed data study (-18.6±3.3 Tg C yr^{-1}, Arrigo et al., 2010) within a similar areal definition of the western Arctic Ocean (Table 3).

We examined the long-term trend of CO_2 sink for each subregion. We found that none of the annual trends computed from observations were significant (Table 1). As CO_2 uptake in the summer accounted for most of the annual sink, we further examined the long-term trends of carbon sink for the summer (Table 2). We found that the observed summer CO_2 sink in the Chukchi Sea significantly increased from 1994 to 2019 by -0.14 ± 0.06 Tg C yr^{-1}, which is confirmed by the modeled result (-0.13 ± 0.03 Tg C yr^{-1}) (Table 2). However, this increasing trend becomes insignificant in the sensitivity test, in which NCP does not increase with time. These results suggested that an increase by 20-30% in NCP is responsible for this long-term increase in summer CO_2 sink in the Chukchi Sea. Such an increase is consistent with the projection that Chukchi Sea would be a larger CO_2 sink based on a recent compilation of pCO$_2$ observations (Ouyang et al., 2020). However, both observation-based and modeled results suggest that the annual CO_2 sink in both the Beaufort Sea and Canada Basin remained unchanged over the years (Table 1). Earlier, Ouyang et al. (2020) predicted that the carbon sink in the Canada Basin would decrease as ΔpCO$_2$ has reduced by 50% over the past two decades. Our further research presented here does not support this prediction as the gradient reduction is compensated by the increased total ice-free area in the Canada Basin. Therefore, we suggest that the change in the air-sea gradient of pCO$_2$ alone may be not enough to reflect the trend of the CO_2 sink in the Arctic Ocean as other factors may also play important roles in controlling the changes in carbon sink. However, once all sea ice is melted in future summers, the predicted trend and the associated mechanism suggested by Ouyang et al. (2020) may still work.

4.2 Climate variability and CO_2 sink responses

To better understand how the CO_2 sink responds to changes in sea ice cover, wind speed, and ΔpCO$_2$ in different regions, we computed the correlation coefficients between the estimated CO_2 sink and possible factors as indicators to identify the main controlling factors for CO_2 sink in each subregion (Table 3). We then examined the temporal variability of these factors to confirm the most likely controlling mechanism (Fig. 8).

The primary controlling factor for the monthly CO_2 sink is the ice-covered area (equivalent to ice%) and the secondary factor is ΔpCO$_2$ in all three subregions. The wind speed only plays a minor role in the Beaufort Sea and Canada Basin and is not significantly correlated to the carbon

sink in the Chukchi Sea (Table 3). Based on this evaluation, we can explain the temporal variation in the estimated carbon sink for each subregion. In the Beaufort Sea, a stronger wind (Fig. 8d) tended to increase gas exchange velocity and hence CO_2 flux. However, the impact of stronger winds appears to be canceled by a reduced ΔpCO_2 (Fig. 8e). More importantly, the relatively stable ice condition (Fig. 8b and c) dominates the interannual variation in regional CO_2 flux (Fig. 8f), which leads the Beaufort Sea to be a relatively stable CO_2 sink over the years. In the Canada Basin, the carbon sink would be expected to decrease with a decline in ΔpCO_2 (Fig. 8e) but a decline in ice% or an increase in open water area (Fig. 8 b and c) offset the expected decrease in CO_2 flux. Thus, no significant change was found in the CO_2 sink in the Canada Basin. Similar mechanisms were noticed in summer months (Fig. 9). The loss of summer sea ice in the Canada Basin and enhanced wind speed in the Beaufort Sea can promote CO_2 uptake and a larger CO_2 sink, but likely compensating for the smaller ΔpCO_2. As a net result, CO_2 sinks do not change significantly from 1994 to 2019 in both the Canada Basin and Beaufort Sea (Fig. 9a). In the Chukchi Sea, our model results suggested that the annual mean ΔpCO_2 significantly shrank over the years (Fig. 8e), which was likely driven by a rapid increase in surface pCO_2 in the late summer and fall (October-November) and strengthened by wind-driven mixing events (Hauri et al., 2013. A similar trend was also reported by Yasunaka et al., (2018). However, this decreased trend of annual ΔpCO_2 did not necessarily translate into a weaker CO_2 flux and CO_2 sink because the annual CO_2 sink was dominated by the extremely high rate of CO_2 uptake in the summer (Fig. 9e). Thus, the annual increase in CO_2 flux (Fig. 8f) and CO_2 sink (Fig. 8a) in the Chukchi Sea were controlled by its summer trends (Fig. 9 a and f). We attributed that primarily to increased primary production (Lewis et al., 2020) that prevents summer pCO_2 from increasing over the years (Fig. 9e) and to earlier sea ice loss and later ice formation with a larger open area that greatly facilitates stronger CO_2 uptake.

4.3 Model limitation and further uncertainty reduction

In our box model, we focused on the main physical and biogeochemical processes determining the carbonate dynamics in the surface mixed layer, such as warming, sea ice loss, and enhanced primary production. The box model enabled us to reconstruct a continued time-series map of sea surface pCO_2 and to establish the possible links between climate variability and the carbon sink response. The model we used for this study appears to be suitable for identifying the main

controlling factors and resolving the complicated relationships among them. However, simplified model settings and multiple assumptions inevitably add uncertainties to both spatial and temporal variations of the various quantities, in particular the final regional CO_2 sinks. The apparent discrepancies between the observation- and model-based estimates highlight the existing challenges in both gap-filling and model forcings (Fig. 8a and Fig. 9a). On the one hand, gap-filling algorithms for observation interpolation are subject to the biases in spatial coverage and the aliases in sample frequency (See section 2.2; Supplementary Tables S6-9), which may lead to over-/under-estimation of interannual variations in CO_2 sink. On the other hand, the box model is forced by the interannual changes of SST, SSS, MLD, sea ice, and wind speed, in combination with the climatological seasonal changes of NCP. Such a setting allows us to capture the first-order seasonality (Fig. 7), at the cost of resolving a partial range of interannual variations of CO_2 sink (Fig. 8a and Fig. 9a). In the current framework, our box model enables us to compare the relative contribution between sea ice and wind speed (Table 3), whereas the discrepancies help us to identify the regions and periods that are most sensitive to observation biases and under-represented forcing.

Here, we would like to discuss some limitations in our current model and possible ways to reduce the uncertainties. Using remote sensing products of SST and sea ice concentration with daily resolution permits us to monitor the rapid changes in SST and sea ice, but we have to rely on an ensemble reanalysis SSS product to reflect the possible lateral and vertical mixing in the water column, seasonal cycle of river discharge, and surface water freshening due to sea ice loss. The current SSS product tended to have a higher surface salinity (by 0.5~2 psu) for summer (July to October). Adjustment of SSS should be done to reduce apparent systematic bias (see Section 2.3.1). We also introduced an E-term (eq (7)) to account for DIC replenishing via respiration and winter ventilation. Coupling with a more skilled physical-driven oceanic model may resolve more dynamic mixing processes, such as eddy transport and shelf-basin interactions, and reduce the large deviation between observed and modeled pCO_2 along the boundaries between the subregions.

Another potential source of the uncertainty of modeled pCO_2 arises from insufficient quantification of NCP. For the Chukchi Sea and Beaufort Sea, we set monthly NCP depending

on several previous studies (Supplementary Table 3) and applied a long-term trend in NCP (Lewis et al., 2020). However, a regional monthly mean NCP does not resolve the highly varied and patchy NCP in the inflow shelf and river-influenced coastal sea. Although we quantified the NCP magnitude based on the assumption that it has a proportional relationship with NPP increase (Lewis et al., 2020), the caveat is that it is not well known how the relationship varies seasonally and regionally. In addition, we used a fixed monthly NCP seasonal cycle which may neglect the observed changes in primary production timing in the Arctic (Song et al., 2021). One possible way to improve our NCP estimate is to incorporate the satellite Chl a data and its derived NCP into the model. However, the satellite data is still limited by sea ice cover in the higher latitude area and the seasonal and spatial variations in NCP remain still poorly known in the western Arctic Ocean. Future improvement of the remote sensing technique is needed to greatly improve the quantification of change in primary production in those areas. This is very challenging as multi-streams of satellite data are currently masked in very high latitudes (e.g., Yasunaka et al., 2018). To deal with this issue, for the first time, we incorporated NCP estimates based on the relationship between ice concentration and NCP into our model for the high latitudes (i.e., Canada Basin). Although these NCP values worked well for simulating seasonal pCO_2 evolution in recent years (2007-2019), we do not have enough pCO_2 and NCP observations in the earlier years (1994-2006) to check whether this relationship is still valid. For future model simulation, multiple approaches for better quantifying NCP in the Arctic Ocean are recommended, including incubation experiments, underway NCP measurements via the $\Delta(O_2/Ar)$ approach, and remote sensing techniques.

5. Summary

In this study, we used a synthesized dataset of sea surface pCO_2 to estimate the CO_2 flux and examine the long-term change in carbon sink for the western Arctic Ocean for the 1994-2019 period. In order to improve spatial and temporal coverage of pCO_2 data, we also performed a data-driven model exercise and produced daily pCO_2 maps with $1° \times 1°$ spatial resolution. Our results show a long-term carbon sink of -18.4 ± 5.5 Tg C yr^{-1} and -22.5 ± 13.8 Tg C yr^{-1} based on observation and model results, respectively, for the entire western Arctic Ocean. Based on pCO_2 observations from 1994 to 2019, we found a significant increasing trend at the rate of -0.14 ± 0.06 Tg C yr^{-1} in summer CO_2 sink in the Chukchi Sea. However, no significant change in CO_2

sink is identified in the Beaufort Sea and Canada Basin, which was corroborated by the modeled results. A closer examination suggested that the long-term trend in annual CO_2 sink was dominated by CO_2 uptake in the summer, thus, modeled results also suggested that the carbon sink in the Chukchi Sea significantly increased by -0.13$\pm$0.05 Tg C yr^{-1}. Using model results allows us to further examine the dominant factors driving the interannual variability of CO_2 flux and carbon sink. For the Chukchi Sea, we attributed the increased carbon sink primarily to a longer ice-free period with a larger open area and increased primary production, and partially to stronger winds. For the Beaufort Sea and Canada Basin, stronger wind and summer active sea ice loss effectively promotes CO_2 uptake but this potential stronger carbon sink is likely to be offset by the smaller $\Delta p CO_2$.

Author contributions: Z. O., Y.L., and W-J. C. prepared the paper. Z. O., W. Z., and Y.W. analyzed the data. Z. O. ran the model simulations. D. Q., A. M., and S. N. contributed data. All authors contributed to discussion and writing.

Competing interests: The authors declare no competing interests.

Data and materials availability: All the data are archived in publicly accessible databases, and the data sources are listed in the main text, Methods and Supplementary Information. The assembled $p CO_2$ dataset used in this study is available in the Supplementary Information. We have submitted the data to PANGEA in February. Here is the link: https://issues.pangaea.de/browse/PDI-27102. We will supply the DOI number upon acceptance.

Reference

Ahmed, M. M., Else, B. G., Capelle, D., Miller, L. A., & Papakyriakou, T. (2020). Underestimation of surface pCO_2 and air-sea CO_2 fluxes due to freshwater stratification in an Arctic shelf sea, Hudson Bay. *Elementa: Science of the Anthropocene*, *8*(1).

Ardyna, M., & Arrigo, K. R. (2020). Phytoplankton dynamics in a changing Arctic Ocean. *Nature Climate Change*, *10*(10), 892-903.

Ardyna, M., Babin, M., Devred, E., Forest, A., Gosselin, M., Raimbault, P., & Tremblay, J. É. (2017). Shelf- basin gradients shape ecological phytoplankton niches and community composition in the coastal Arctic Ocean (Beaufort Sea). *Limnology and oceanography*, *62*(5), 2113-2132.

Arrigo, K. R., Pabi, S., van Dijken, G. L., & Maslowski, W. (2010). Air- sea flux of CO_2 in the Arctic Ocean, 1998–2003. *Journal of Geophysical Research: Biogeosciences*, *115*(G4). https://doi.org/10.1029/2009JG001,224

Bakker, D. C., Pfeil, B., Landa, C. S., Metzl, N., O'brien, K. M., Olsen, A., ... & Xu, S. (2016). A multi-decade record of high-quality fCO_2 data in version 3 of the Surface Ocean CO_2 Atlas (SOCAT). *Earth System Science Data*, *8*(2), 383-413.

Bates, N. R., Moran, S. B., Hansell, D. A., & Mathis, J. T. (2006). An increasing CO_2 sink in the Arctic Ocean due to sea- ice loss. *Geophysical Research Letters*, *33*(23). http://dx.doi.org/10.1029/2006GL027028.

Bates, N. R., & Mathis, J. T. (2009). The Arctic Ocean marine carbon cycle: evaluation of air-sea CO_2 exchanges, ocean acidification impacts and potential feedbacks. *Biogeosciences*, *6*(11), 2433-2459. https://doi.org/10.5194/bg-6-2433-2009

Buck, A. L. (1981). New equations for computing vapor pressure and enhancement factor. *Journal of Applied Meteorology and Climatology*, *20*(12), 1527-1532.

Butterworth, B. J., & Miller, S. D. (2016). Air- sea exchange of carbon dioxide in the Southern Ocean and Antarctic marginal ice zone. *Geophysical Research Letters*, *43*(13), 7223-7230. doi:10.1002/2016GL069581.

Cai, W. J., Chen, L., Chen, B., Gao, Z., Lee, S. H., Chen, J., ... & Zhang, H. (2010). Decrease in the CO2 uptake capacity in an ice-free Arctic Ocean basin. *Science, 329*(5991), 556-559.

Cai, W. J., Bates, N. R., Guo, L., Anderson, L. G., Mathis, J. T., Wanninkhof, R., ... & Semiletov, I. P. (2014). Carbon fluxes across boundaries in the Pacific Arctic region in a changing environment. In The Pacific Arctic Region (pp. 199-222). Springer, Dordrecht.

Chen, B., Cai, W. J., & Chen, L. (2015). The marine carbonate system of the Arctic Ocean: assessment of internal consistency and sampling considerations, summer 2010. *Marine Chemistry*, *176*, 174-188.

Comiso, J. C. (2017). Bootstrap Sea Ice Concentrations from Nimbus-7 SMMR and DMSP SSM/I-SSMIS, Version 3. Boulder, Colorado USA. NASA National Snow and Ice Data Center Distributed Active Archive Center. doi: https://doi.org/10.5067/7Q8HCCWS4I0R.

Else, B. G. T., Papakyriakou, T. N., Galley, R. J., Mucci, A., Gosselin, M., Miller, L. A., ... & Thomas, H. (2012). Annual cycles of pCO_2sw in the southeastern Beaufort Sea: New understandings of air- sea CO_2 exchange in arctic polynya regions. *Journal of Geophysical Research: Oceans*, *117*(C9).

Else, B. G., Galley, R. J., Lansard, B., Barber, D. G., Brown, K., Miller, L. A., ... & Rysgaard, S. (2013). Further observations of a decreasing atmospheric CO_2 uptake capacity in the Canada Basin (Arctic Ocean) due to sea ice loss. *Geophysical Research Letters*, *40*(6), 1132-1137.

Evans, W., Mathis, J., Cross, J., Bates, N., Frey, K., Else, B., et al. (2015). Sea-air CO_2 exchange in the western Arctic coastal ocean. *Global Biogeochemical Cycles, 29*(8), 1190-1209. doi:10.1002/2015GB005153

Fransson, A., Chierici, M., Skjelvan, I., Olsen, A., Assmy, P., Peterson, A. K., ... & Ward, B. (2017). Effects of sea- ice and biogeochemical processes and storms on under- ice water fCO_2 during the winter- spring transition in the high Arctic Ocean: Implications for sea- air CO_2 fluxes. *Journal of Geophysical Research: Oceans*, *122*(7), 5566-5587.

Gattuso J.-P., Epitalon J.-M., Lavigne H. & Orr J., 2018. seacarb: seawater carbonate chemistry. R package version 3.2.10. http://CRAN.R-project.org/package=seacarb

Gloege, L., McKinley, G. A., Landschützer, P., Fay, A. R., Frölicher, T. L., Fyfe, J. C., ... & Takano, Y. (2020). Quantifying errors in observationally- based estimates of ocean carbon sink variability. *Global Biogeochemical Cycles*, e2020GB006788.

Hauri, C., Winsor, P., Juranek, L. W., McDonnell, A. M., Takahashi, T., & Mathis, J. T. (2013). Wind- driven mixing causes a reduction in the strength of the continental shelf carbon pump in the Chukchi Sea. *Geophysical Research Letters*, *40*(22), 5932-5936.

Ji, B., Sandwith, Z., Williams, W., Diaconescu, O., Ji, R., Li, Y., et al. (2019). Variations in rates of biological production in the Beaufort Gyre as the Arctic changes: Rates from 2011 to 2016. *Journal of Geophysical Research: Oceans, 124*(6), 3628-3644. doi:10.1029/2018JC014805

Landschützer, P., Gruber, N., Bakker, D. C. E., Schuster, U., Nakaoka, S., Payne, M. R., et al. (2013). A neural network- based estimate of the seasonal to inter- annual variability of the

Atlantic Ocean carbon sink. *Biogeosciences, 10*(11), 7793–7815. https://doi.org/10.5194/bg-10- 7793- 2013

Landschützer, P., Gruber, N., Bakker, D. C. E., & Schuster, U. (2014). Recent variability of the global ocean carbon sink. *Global Biogeochemical Cycles, 28*, 927–949. https://doi.org/10.1002/2014GB004853

Landschützer, P., Gruber, N., & Bakker, D. C. E. (2016). Decadal variations and trends of the global ocean carbon sink. *Global Biogeochemical Cycles, 30*, 1396–1417. https://doi.org/10.1002/2015GB005359

Laruelle, G. G., Lauerwald, R., Pfeil, B., & Regnier, P. (2014). Regionalized global budget of the CO_2 exchange at the air- water interface in continental shelf seas. *Global Biogeochemical Cycles, 28*, 1199–1214. https://doi.org/10.1002/2014GB004832

Laruelle, G. G., Landschützer, P., Gruber, N., Tison, J. L., Delille, B., & Regnier, P. (2017). Global high- resolution monthly pCO2 climatology for the coastal ocean derived from neural network interpolation. *Biogeosciences, 14*(19), 4545–4561. https://doi.org/10.5194/bg- 14- 4545- 2017

Lewis, K. M., van Dijken, G. L., & Arrigo, K. R. (2020). Changes in phytoplankton concentration now drive increased Arctic Ocean primary production. *Science, 369*(6500), 198-202.

Loose, B., McGillis, W., Perovich, D., Zappa, C., & Schlosser, P. (2014). A parameter model of gas exchange for the seasonal sea ice zone. *Ocean Science, 10*(1), 17-17. doi:10.5194/os-10-17-2014

Lovely, A., Loose, B., Schlosser, P., McGillis, W., Zappa, C., Perovich, D., et al. (2015), The Gas Transfer through Polar Sea ice experiment: Insights into the rates and pathways that determine geochemical fluxes, *Journal of Geophysical Research: Oceans, 120*, 8177–8194, doi:10.1002/2014JC010607.

Manizza, M., Follows, M. J., Dutkiewicz, S., Menemenlis, D., Hill, C. N., & Key, R. M. (2013). Changes in the Arctic Ocean CO_2 sink (1996–2007): A regional model analysis. *Global Biogeochemical Cycles, 27*, 1108–1118. https://doi.org/10.1002/2012GB004491

Manizza, M., Menemenlis, D., Zhang, H., & Miller, C. E. (2019). Modeling the recent changes in the Arctic Ocean CO_2 sink (2006–2013). *Global Biogeochemical Cycles, 33*(3), 420-438.

Mathis, J. T., Pickart, R. S., Byrne, R. H., McNeil, C. L., Moore, G. W. K., Juranek, L. W., ... & Feely, R. A. (2012). Storm- induced upwelling of high pCO$_2$ waters onto the continental shelf of the western Arctic Ocean and implications for carbonate mineral saturation states. *Geophysical Research Letters*, *39*(7).

Miller, L. A., Burgers, T. M., Burt, W. J., Granskog, M. A., & Papakyriakou, T. N. (2019). Air-Sea CO$_2$ flux estimates in stratified Arctic coastal waters: How wrong can we be?. *Geophysical Research Letters*, *46*(1), 235-243.

Millero, F. J., T. B. Graham, F. Huang, H. Bustos-Serrano, and D. Pierrot (2006), Dissociation constants of carbonic acid in seawater as a function of salinity and temperature, *Mar. Chem., 100*, 80–94.

Murata, A., &Takizawa, T. (2003). Summertime CO$_2$ sink in shelf and slope waters of the western Arctic Ocean. *Continental Shelf Research, 23*, 753–776.

Olsen, A., Lange, N., Key, R. M., Tanhua, T., Bittig, H. C., Kozyr, A., ... & Woosley, R. J. (2020). GLODAPv2. 2020–the second update of GLODAPv2. *Earth System Science Data*.

Ouyang, Z., Qi, D., Chen, L., Takahashi, T., Zhong, W., DeGrandpre, M. D., ... & Sun, H. (2020). Sea-ice loss amplifies summertime decadal CO$_2$ increase in the western Arctic Ocean. *Nature Climate Change, 10*(7), 678-684.

Ouyang, Z., Qi, D., Zhong, W., Chen, L., Gao, Z., Lin, H., ... & Cai, W. J. (2021). Summertime evolution of net community production and CO$_2$ flux in the western Arctic Ocean. *Global Biogeochemical Cycles*, e2020GB006651.

Peng, G., Meier, W., Scott, D., Savoie, M., A long-term and reproducible passive microwave sea ice concentration data record for climate studies and monitoring. *Earth Syst. Sci. Data, 5*, 311e318 (2013).

Prytherch, J., Brooks, I., Crill, P., Thornton, B., Salisbury, D., Tjernström, M., et al. (2017). Direct determination of the air-sea CO$_2$ gas transfer velocity in Arctic sea ice regions. *Geophysical Research Letters, 44*(8), 3770-3778. doi:10.1002/2017GL073593

Randelhoff A, Holding J, Janout M, Sejr MK, Babin M, Tremblay J-É and Alkire MB (2020) Pan-Arctic Ocean Primary Production Constrained by Turbulent Nitrate Fluxes. *Front. Mar. Sci.* 7:150. doi: 10.3389/fmars.2020.00150

Roobaert, A., Laruelle, G. G., Landschützer, P., Gruber, N., Chou, L., & Regnier, P. (2019). The spatiotemporal dynamics of the sources and sinks of CO$_2$ in the global coastal ocean. *Global Biogeochemical Cycles, 33*(12), 1693-1714.

Shadwick, E. H., Thomas, H., Chierici, M., Else, B., Fransson, A., Michel, C., ... & Tremblay, J. É. (2011). Seasonal variability of the inorganic carbon system in the Amundsen Gulf region of the southeastern Beaufort Sea. *Limnology and Oceanography, 56*(1), 303-322.

Song, H, R. Ji, M. Jin, Y. Li, Z. Feng, O., Varpe, and C. Davis (in final revision), Strong and regionally distinct links between sea-ice phenology and primary production in the Arctic, *Limnology and Oceanography.* In press.

Takahashi, T., Sutherland, S. C., Wanninkhof, R., Sweeney, C., Feely, R. A., Chipman, D. W., ... & Watson, A. (2009). Climatological mean and decadal change in surface ocean pCO_2, and net sea–air CO_2 flux over the global oceans. *Deep Sea Research Part II: Topical Studies in Oceanography, 56*(8-10), 554-577.

Tremblay, J.-É. et al. Impact of river discharge, upwelling and vertical mixing on the nutrient loading and productivity of the Canadian Beaufort Shelf. Biogeosciences 11, 4853–4868 (2014).

Tu, Z., Le, C., Bai, Y., Jiang, Z., Wu, Y., Ouyang, Z., ... & Qi, D. (2021). Increase in CO2 Uptake Capacity in the Arctic Chukchi Sea During Summer Revealed by Satellite- Based Estimation. *Geophysical Research Letters*, *48*(15), e2021GL093844.

Wanninkhof, R. (2014). Relationship between wind speed and gas exchange over the ocean revisited. *Limnology and Oceanography: Methods, 12*(6), 351-362. doi:10.4319/lom.2014.12.351

Weiss, R. (1974). Carbon dioxide in water and seawater: The solubility of a non-ideal gas. *Marine Chemistry, 2*(3), 203-215. doi:10.1016/0304-4203(74)90015-2

Woodgate, R., Weingartner, T., & Lindsay, R. (2012). Observed increases in Bering Strait oceanic fluxes from the Pacific to the Arctic from 2001 to 2011 and their impacts on the Arctic Ocean water column. *Geophysical Research Letters, 39*(24). doi:10.1029/2012GL054092

Woodgate, R. A. (2018). Increases in the Pacific inflow to the Arctic from 1990 to 2015, and insights into seasonal trends and driving mechanisms from year-round Bering Strait mooring data. *Progress in Oceanography, 160*, 124-154. doi:10.1016/j.pocean.2017.12.007

Woosley, R. J., Millero, F. J. & Takahashi, T. Internal consistency of the inorganic carbon system in the Arctic Ocean. *Limnol. Oceanogr. Methods, 15*, 887–896 (2017).

Yasunaka, S., Murata, A., Watanabe, E., Chierici, M., Fransson, A., van Heuven, S., et al. (2016). Mapping of the air-sea CO_2 flux in the arctic ocean and its adjacent seas: Basin-wide

distribution and seasonal to interannual variability. *Polar Science, 10*(3), 323–334. https://doi.org/10.1016/j.polar.2016.03.006

Yasunaka, S., Siswanto, E., Olsen, A., Hoppema, M., Watanabe, E., Fransson, A., ... & Mathis, J. T. (2018). Arctic Ocean CO_2 uptake: an improved multiyear estimate of the air–sea CO_2 flux incorporating chlorophyll a concentrations. *Biogeosciences*, *15*(6), 1643-1661.

Zheng, Z., Wei, H., Luo, X., & Zhao, W. (2021a). Mechanisms of Persistent High Primary Production During the Growing Season in the Chukchi Sea. *Ecosystems*, *24*(4), 891-910.

Zheng, Z., Luo, X., Wei, H., Zhao, W., & Qi, D. (2021b). Analysis of the Seasonal and Interannual Variations of Air‐ Sea CO_2 Flux in the Chukchi Sea Using A Coupled Ocean‐ Sea Ice‐ Biogeochemical Model. *Journal of Geophysical Research: Oceans*, e2021JC017550.
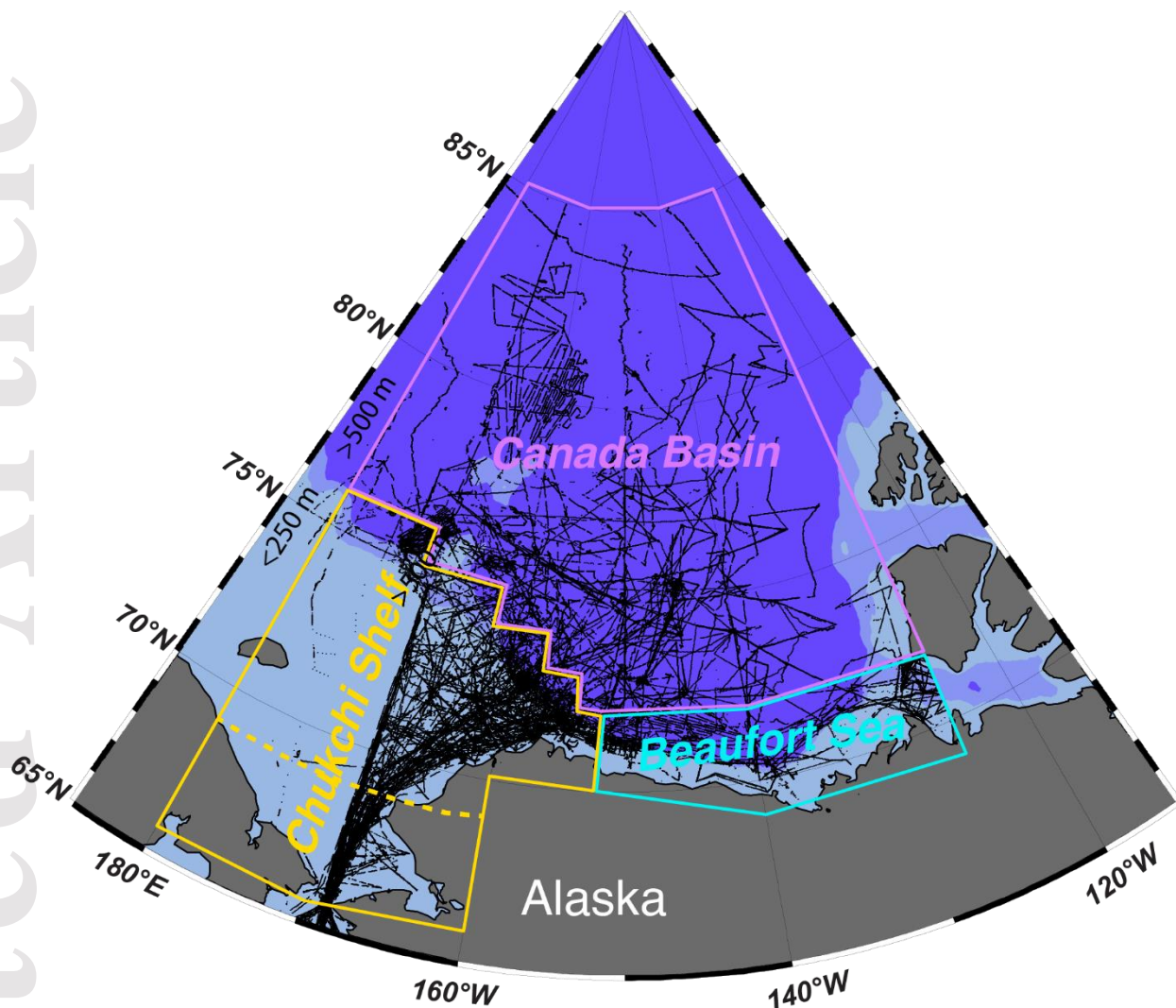
Figure 1. The western Arctic Ocean map with bathymetry information (<250 m, 250-500 m, and >500 m). Black lines indicate the cruise tracks of the sea surface pCO2 measurements through 1994 to 2019. We divided the western Arctic Ocean into three subregions (a): (1) Chukchi Sea shelf (CS), which sometimes further divided into the southern Chukchi Shelf (sCS, 65°N–69°N) and the northern Chukchi Shelf (nCS, >69°N), as shown by the yellow dash line; (2) Canada Basin (CB), separated from the Chukchi Shelf mainly along the 250-500 m isobaths; (3) the coastal Beaufort Sea (BS), separated from the Chukchi Sea and Canada Basin along 152°W and 72°N, respectively. Figure was produced by Ocean Data View (Schlitzer, 2018).
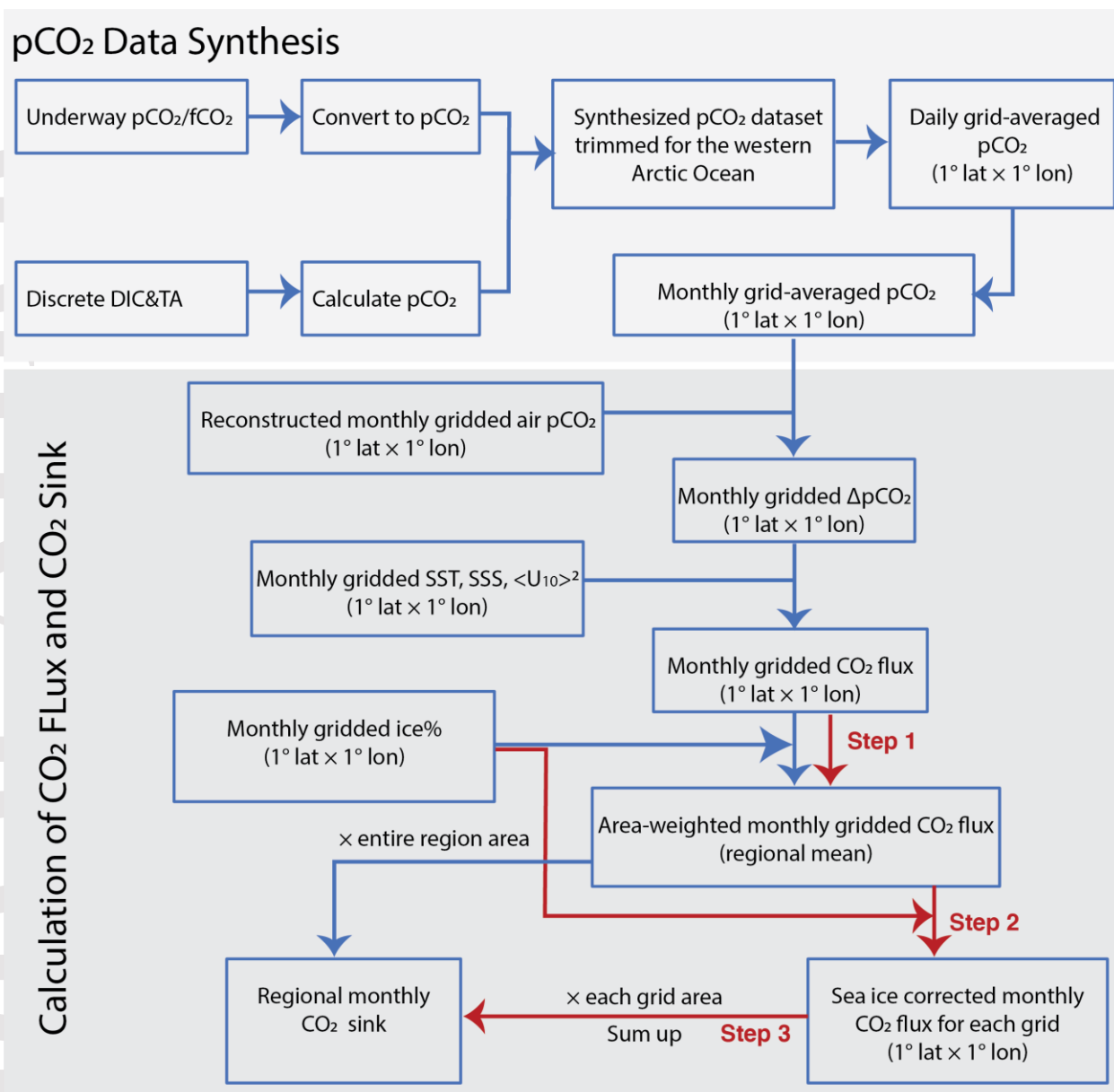
Figure 2. Synthesis of pCO_2 datasets and calculation of monthly CO_2 flux and CO_2 sink. The blue arrows indicate the approaches used in Laruelle et al., (2014) and Evans et al., (2015). Our modifications of CO_2 sink calculation are highlighted by red arrows.
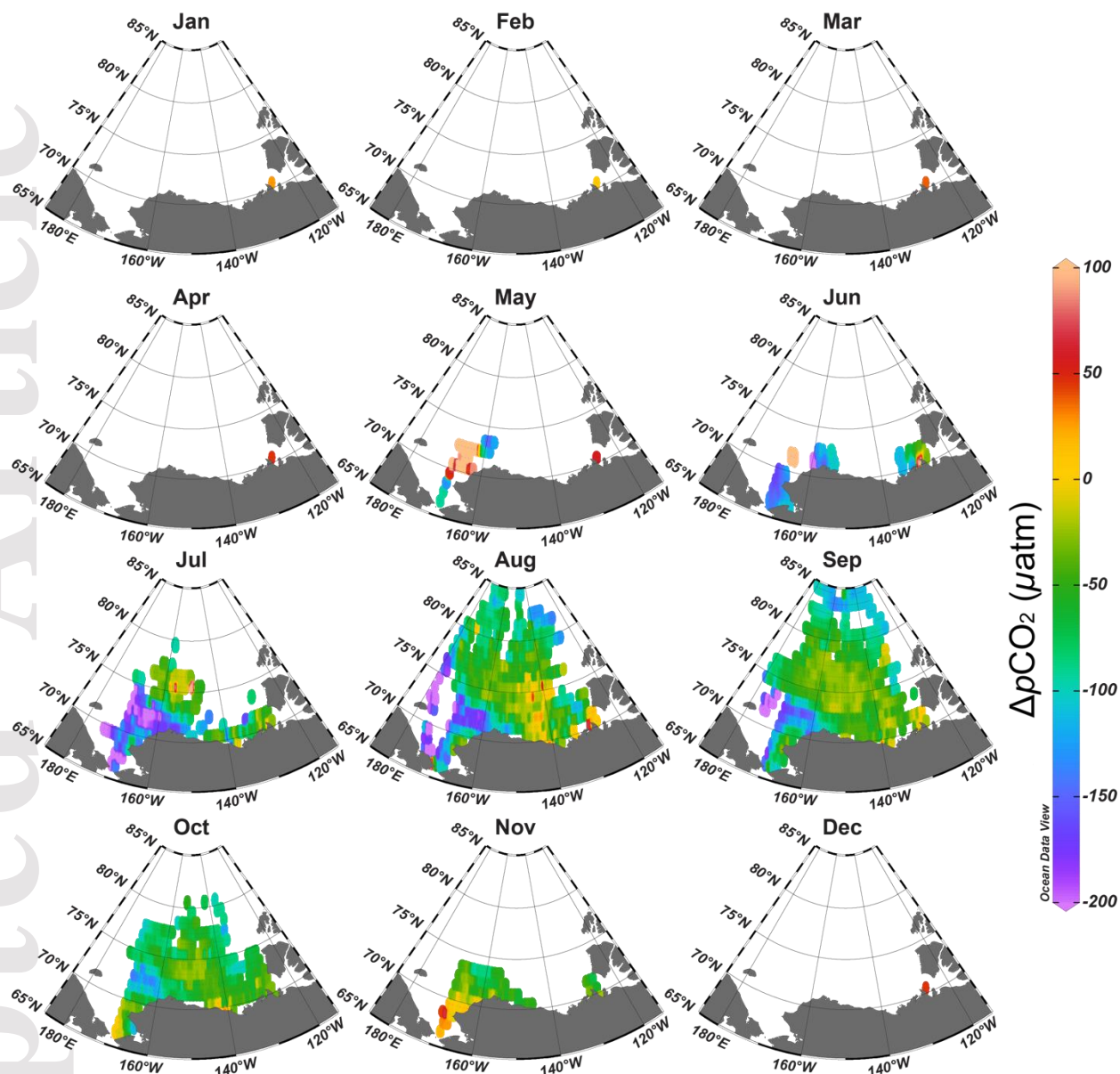
Figure 3. Observation-based monthly climatology of $\Delta p\mathrm{CO}_2$ in 1°×1° grids in the western Arctic Ocean. $\Delta p\mathrm{CO}_2$ is defined as $p\mathrm{CO}_2^{\mathrm{sea}} - p\mathrm{CO}_2^{\mathrm{air}}$ and negative values of $\Delta p\mathrm{CO}_2$ indicate that sea surface $p\mathrm{CO}_2$ is lower than the atmospheric $p\mathrm{CO}_2$.

Figure 4. Observation-based monthly climatology of CO_2 flux in 1°×1° grids in the western Arctic Ocean. Negative values of CO_2 flux values indicate that CO_2 uptake from the atmosphere.
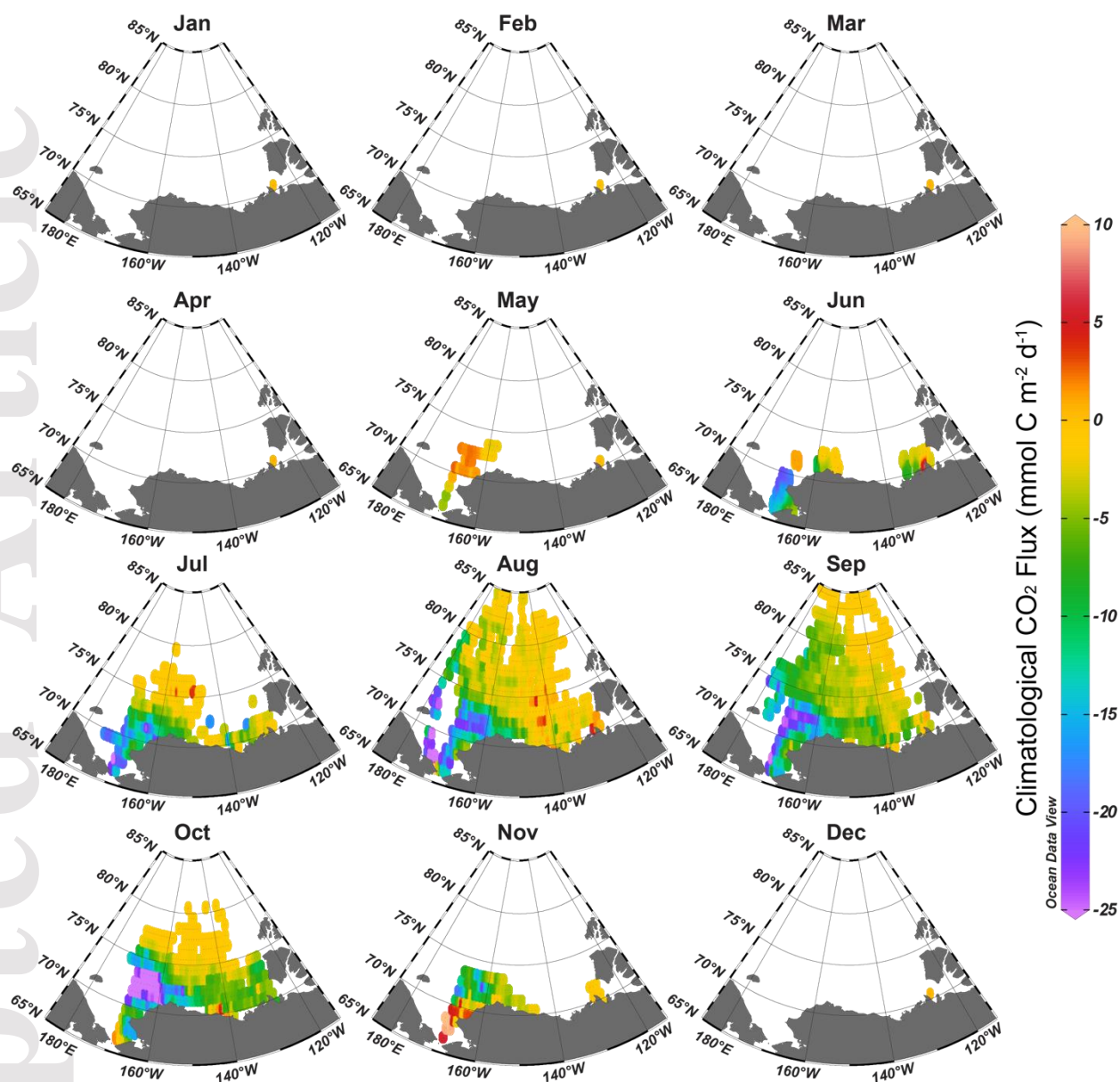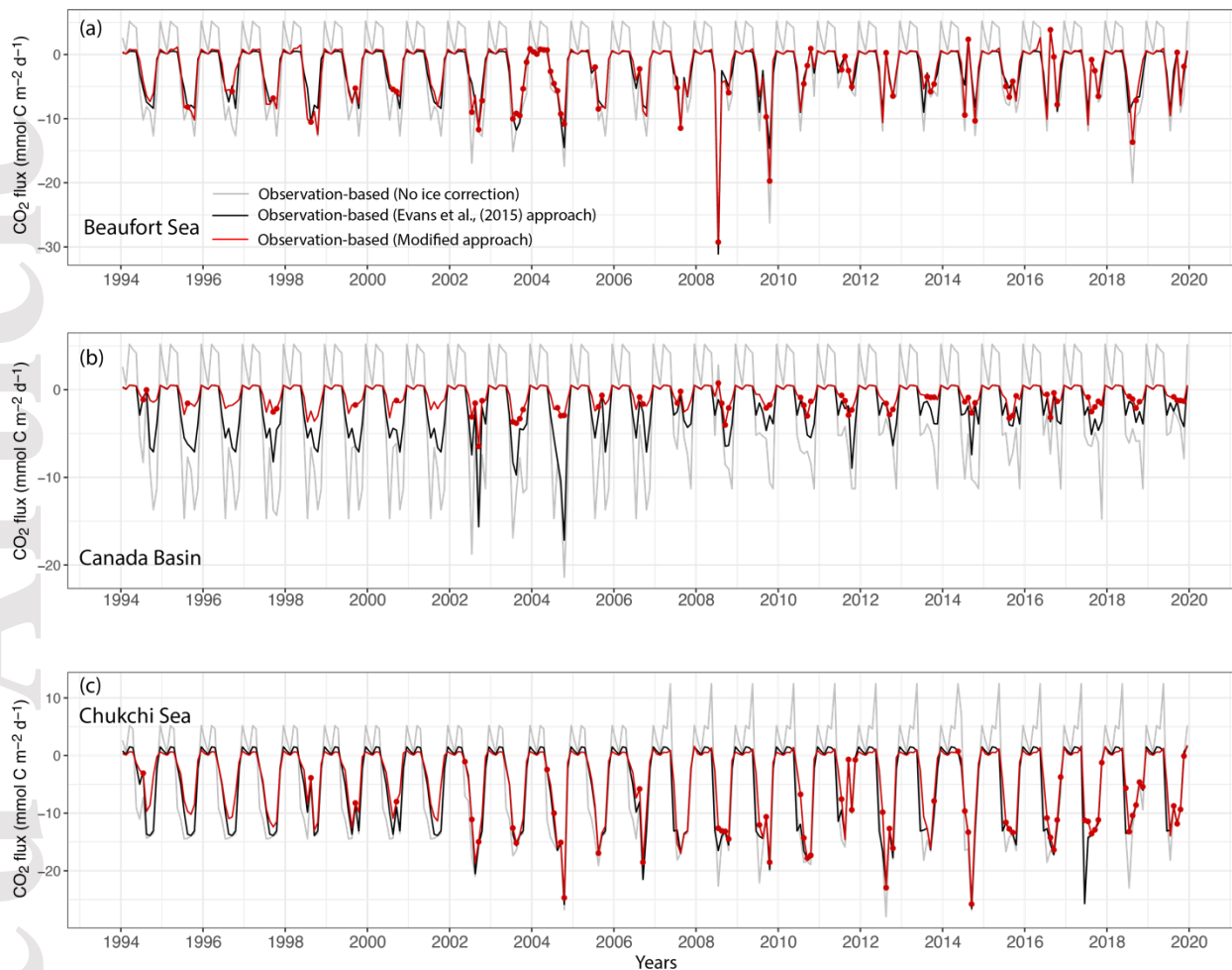
Figure 5. Temporal variations of CO_2 flux in the (a) Beaufort Sea, (b) Canada Basin, and (c) Chukchi Sea. Grey, black and red lines represent monthly CO_2 fluxes based on observations, estimated by using the approach of no ice correction, ice correction described in Evans et al., (2015) and modified ice correction in this study, respectively. Red dots show the months, in which observations are available. For those months without any observations, we reconstructed monthly CO_2 flux with climatological monthly means separately for the periods of 1994-2006 and 2007-2019 (See Supplementary Tables S6-9). Note that negative values of CO_2 flux indicate CO_2 uptake from the atmosphere.
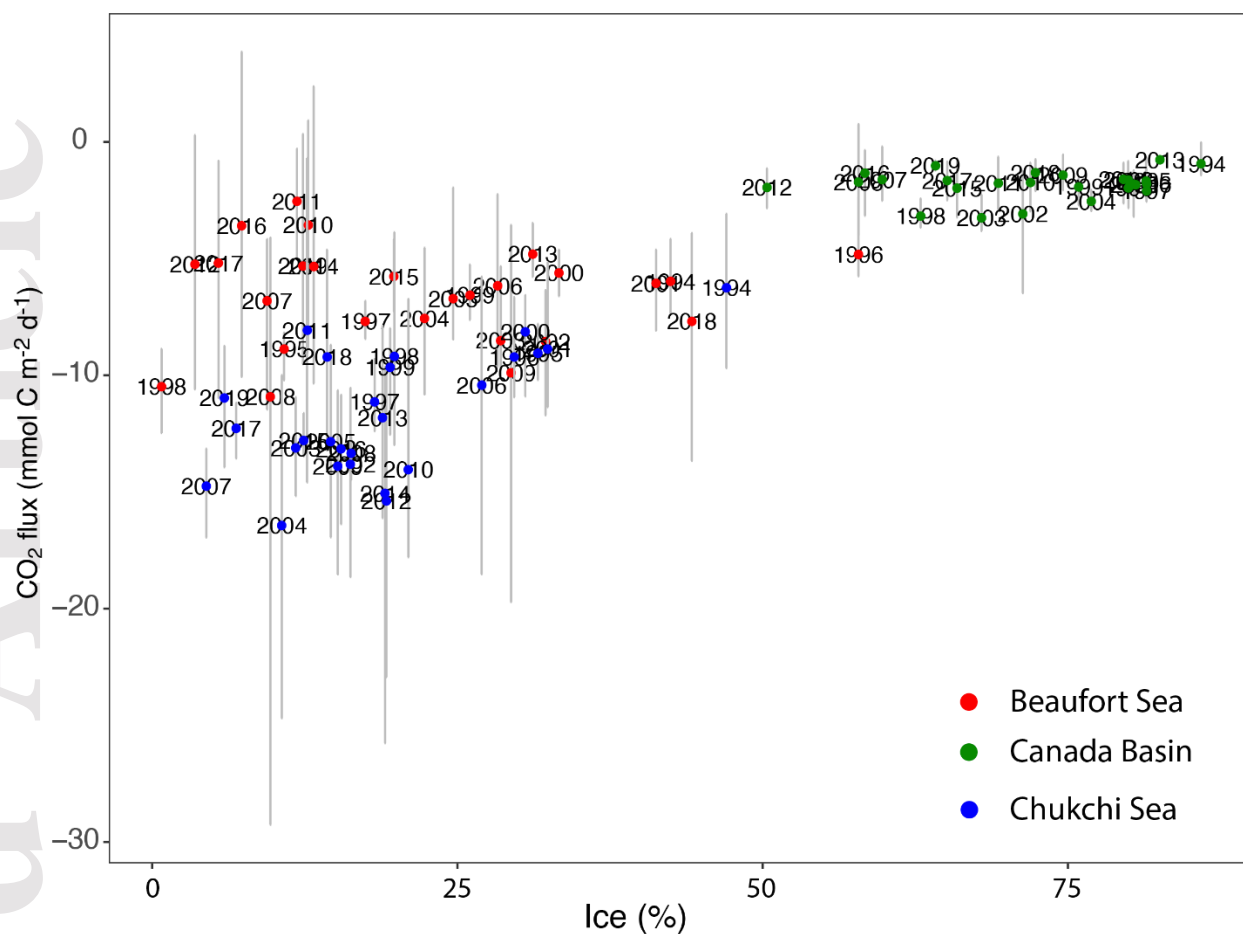
Figure 6. Regional CO_2 flux versus ice concentration in summer (July to October). The colored dots represent the summer means of CO_2 flux in the Beaufort Sea (red), Canada Basin (green) and Chukchi Sea (blue) in a particular year. The error bars (grey) associated with the data represent the seasonal variability, reported as the highest and lowest monthly values through July to October for a given subregion.
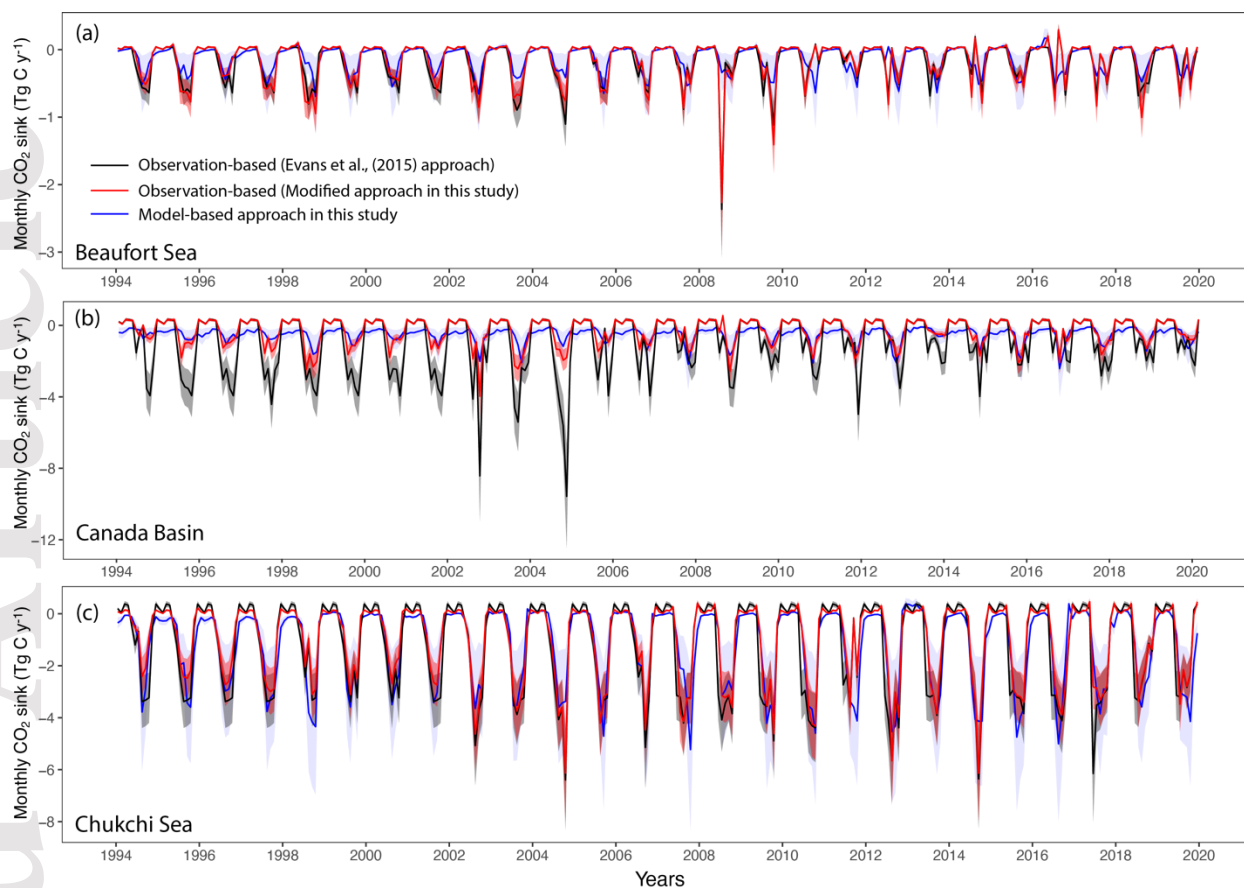
Figure 7. Temporal variations in the CO_2 sink in the (a) Beaufort Sea, (b) Canada Basin, and (c) Chukchi Sea. Red lines indicate the observation-based carbon sink changes, estimated using the modified approach described in this study. Blue lines indicate the modeled-based estimates. The shaded areas correspond to the uncertainties of carbon sink estimation (see Section 2.5).
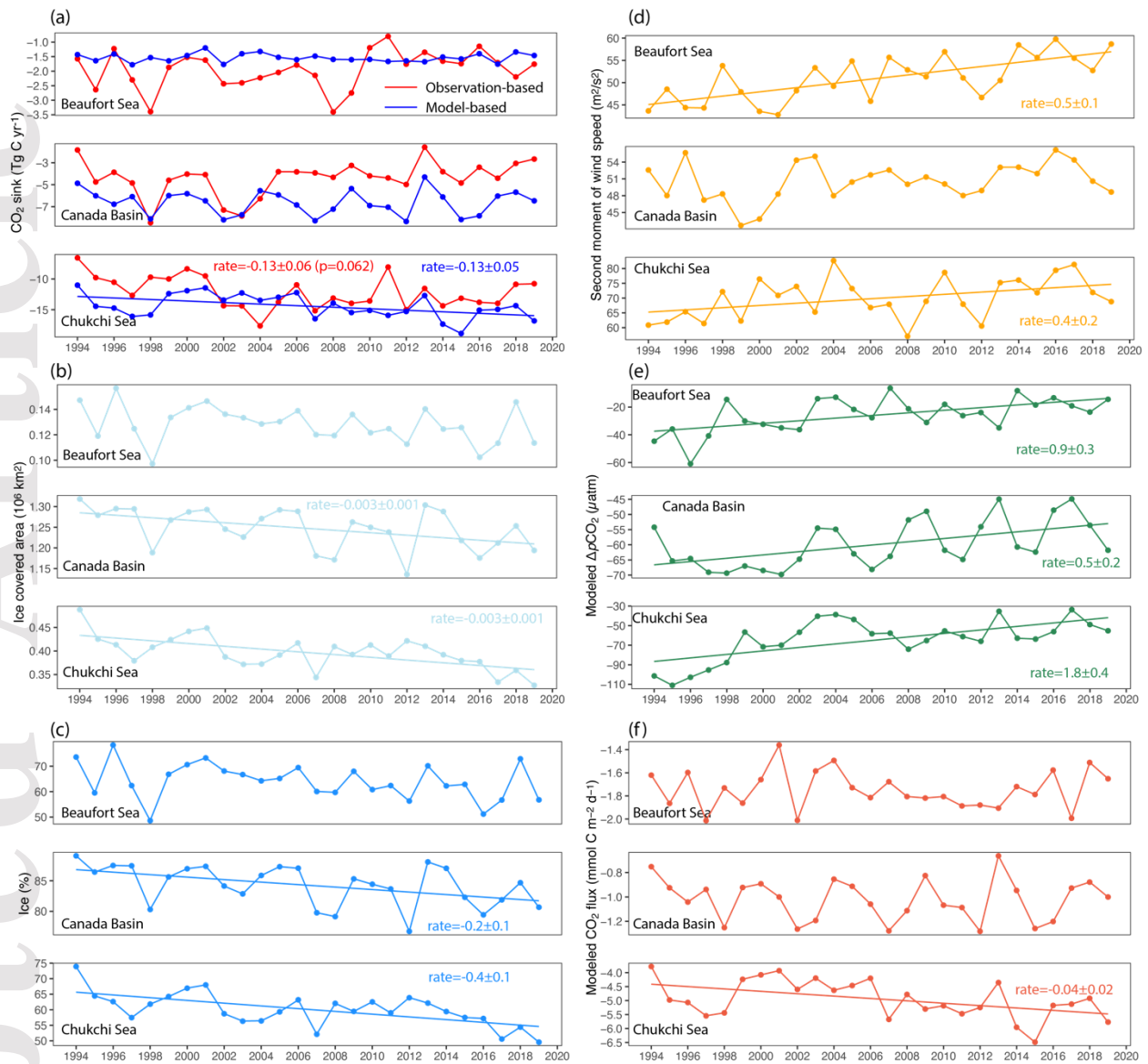
Figure 8. Interannual variation in CO_2 sinks (a) and other associated variables (b-f). We tested whether the trends were significantly different from 0 by conducting an analysis of variance (ANOVA); only the significant rates (changes per year, p<0.05) are shown.
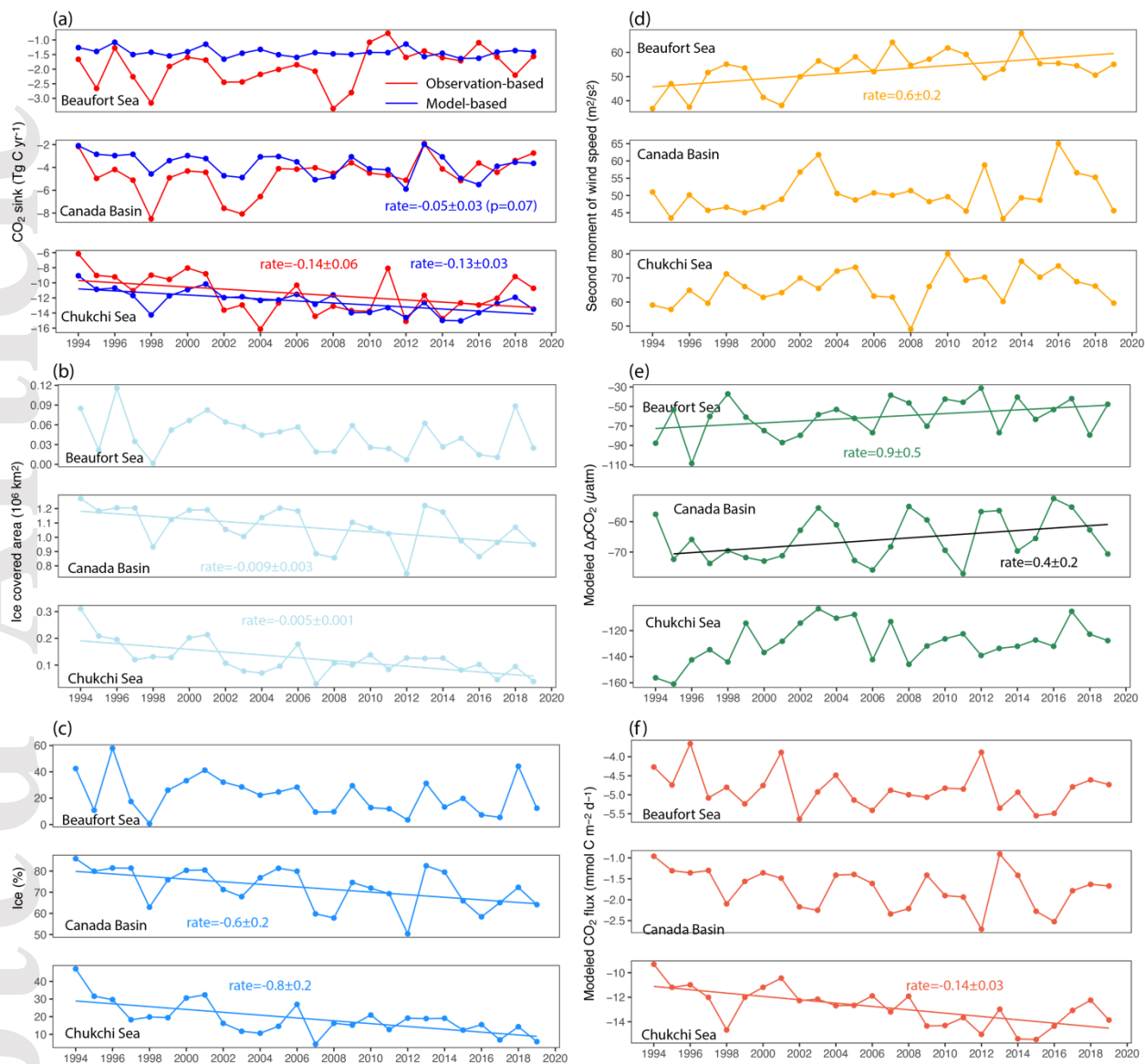
Figure 9. Interannual variation (summer only; July-October) in carbon sinks (a) and other associated variables (b-f). We tested whether the trends were significantly different from 0 by conducting an analysis of variance (ANOVA). Only the significant rates (changes per year, $p<0.05$) are shown. Note that the trend of modeled $\Delta p CO_2$ in the Canada Basin is significant when we excluded the point in 1994.

Table 1. Regional annual and summer (July-October) CO_2 sink (Tg C yr^{-1}). Negative sign denotes a CO_2 flux from the atmosphere into the ocean. The surface areas of each subregion are 0.20×10^6 km^2 for the Beaufort Sea, 1.48×10^6 km^2 for the Canada Basin, and 0.66×10^6 km^2 for the Chukchi Sea. ANOVA was performed to test whether the yearly change calculated for 1994-2019 was significantly different from 0. The asterisks indicate the significance level of the trends (*$P < 0.05$).

year	Beaufort Sea Annual Obs-based[a]	Annual Modeled	Summer Obs-based[a]	Summer Modeled	Canada Basin Annual Obs-based[a]	Annual Modeled	Summer Obs-based[a]	Summer Modeled	Chukchi Sea Annual Obs-based[a]	Annual Modeled[b]	Annual Modeled[c]	Summer Obs-based[a]	Summer Modeled[b]	Summer Modeled[c]
1994	-1.6	-1.4	-1.7	-1.3	-1.8	-4.9	-2.2	-2.1	-6.6	-11.0	-11.0	-6.2	-9.1	-9.1
1995	-2.6	-1.6	-2.7	-1.4	-4.7	-6.0	-5.0	-2.8	-9.8	-14.5	-14.4	-9.0	-10.9	-10.9
1996	-1.2	-1.4	-1.3	-1.1	-3.9	-6.8	-4.2	-3.0	-10.5	-14.7	-14.7	-9.2	-10.7	-10.7
1997	-2.3	-1.8	-2.3	-1.5	-4.8	-6.1	-5.1	-2.8	-12.7	-16.1	-16.1	-11.0	-11.7	-11.7
1998	-3.4	-1.5	-3.2	-1.4	-8.5	-8.1	-8.5	-4.6	-9.7	-15.8	-15.8	-9.0	-14.3	-14.3
1999	-1.9	-1.6	-1.9	-1.5	-4.6	-6.0	-4.9	-3.4	-10.0	-12.4	-12.3	-9.6	-11.7	-11.6
2000	-1.5	-1.5	-1.6	-1.4	-4.0	-5.8	-4.3	-3.0	-8.3	-11.9	-11.7	-8.0	-10.9	-10.7
2001	-1.6	-1.2	-1.7	-1.1	-4.1	-6.5	-4.4	-3.2	-9.5	-11.4	-11.1	-8.8	-10.2	-9.9
2002	-2.4	-1.8	-2.4	-1.7	-7.3	-8.2	-7.6	-4.7	-14.3	-13.4	-13.0	-13.6	-12.0	-11.5
2003	-2.4	-1.4	-2.4	-1.5	-7.8	-7.8	-8.1	-4.9	-14.4	-12.3	-11.7	-12.9	-11.8	-11.3
2004	-2.2	-1.3	-2.2	-1.3	-6.3	-5.5	-6.6	-3.1	-17.6	-13.5	-12.7	-16.1	-12.3	-11.6
2005	-2.0	-1.5	-2.0	-1.5	-3.8	-5.9	-4.1	-3.0	-13.8	-13.0	-12.2	-12.7	-12.3	-11.4
2006	-1.8	-1.6	-1.8	-1.6	-3.8	-6.8	-4.2	-3.5	-11.0	-12.2	-11.5	-10.3	-11.5	-10.7
2007	-2.1	-1.5	-2.1	-1.4	-3.9	-8.3	-4.0	-5.1	-15.2	-16.5	-15.2	-14.4	-12.9	-11.7
2008	-3.4	-1.6	-3.3	-1.5	-4.3	-7.2	-4.5	-4.8	-13.1	-13.9	-12.8	-13.1	-11.6	-10.6
2009	-2.8	-1.6	-2.8	-1.5	-3.3	-5.4	-3.6	-3.1	-14.0	-15.4	-13.9	-13.7	-14.0	-12.5
2010	-1.2	-1.7	-1.1	-1.4	-4.2	-6.9	-4.5	-4.1	-13.6	-15.1	-13.6	-13.8	-13.9	-12.4
2011	-0.8	-1.6	-0.8	-1.4	-4.4	-7.1	-4.7	-4.2	-8.1	-15.9	-14.2	-8.1	-13.3	-11.6
2012	-1.8	-1.7	-1.6	-1.1	-5.0	-8.4	-5.1	-5.9	-15.0	-15.3	-13.6	-15.1	-14.6	-12.9
2013	-1.3	-1.7	-1.4	-1.6	-1.6	-4.3	-1.9	-2.0	-11.6	-12.7	-11.0	-11.7	-12.6	-10.9
2014	-1.7	-1.5	-1.6	-1.5	-3.8	-6.1	-4.1	-3.1	-14.4	-17.4	-15.1	-14.7	-15.0	-12.8
2015	-1.7	-1.6	-1.7	-1.6	-4.8	-8.2	-5.2	-4.9	-13.1	-18.9	-16.3	-12.7	-15.0	-12.8
2016	-1.1	-1.4	-1.1	-1.6	-3.4	-7.8	-3.6	-5.5	-13.8	-15.1	-12.9	-12.9	-14.0	-11.8
2017	-1.7	-1.8	-1.6	-1.4	-4.4	-6.0	-4.4	-3.9	-14.0	-15.0	-12.8	-12.0	-12.7	-10.5
2018	-2.2	-1.3	-2.2	-1.4	-3.1	-5.7	-3.4	-3.5	-10.9	-14.3	-12.4	-9.2	-11.9	-9.8
2019	-1.8	-1.5	-1.6	-1.4	-2.7	-6.5	-2.7	-3.6	-10.8	-16.8	-14.2	-10.7	-13.5	-10.9
Mean ± uncertainty	-1.9±0.6	-1.5±1.2	-1.9±0.6	-1.4±1.2	-4.4±1.3	-6.6±4.0	-4.6±1.4	-3.8±2.1	-12.1±3.6	-14.4±8.6	-13.3±8.0	-11.5±3.5	-12.5±7.5	-11.4±6.8
Yearly change ± standard error	0.02±0.02	-0.001±0.004	0.03±0.02	-0.005±0.004	0.07±0.04	-0.01±0.03	0.07±0.04	-0.05±0.03	-0.13±0.06	-0.13±0.05*	-0.01±0.04	-0.14±0.06*	-0.13±0.03*	-0.02±0.03

[a] Carbon sink was estimated using the modified approach described in this study.
[b] Modeled carbon sink with applying an increased rate of NCP.
[c] Modeled carbon sink without applying an increased rate of NCP.

Table 2. Estimates of the air-sea CO_2 flux and carbon sink in the western Arctic Ocean.

Region	Period	Air-sea CO_2 flux (mmol C m^{-2} d^{-1})	Annual CO_2 sink (Tg C yr^{-1})	Method	Reference
Beaufort Sea	1994-2019	-2.2±0.7	-1.9±0.6	Observation	This study
	1994-2019	-1.7±1.4	-1.5±1.2	Box-model	This study
	2006-2013	-1.0±0.6	-4.3±2.5	Biogeochemical Model	Manizza et al. (2019)
	2003-2014	-1.0	-4.0	Observation	Evans et al. (2015)
	1996-2007		-0.9±0.5	Biogeochemical Model	Manizza et al. (2013)
	1998-2003		-9.1±2.4*	Multiple linear regression with remote sensing data	Arrigo et al. (2010)
	1998-2000	-12.0	-2.0	Observation	Murata and Takizawa (2003)
Canada Basin	1994-2019	-0.6±0.2	-4.4±1.3	Observation	This study
	1994-2019	-1.0±0.7	-6.6 ± 4.0	Box-model	This study
	2006-2013	0	+0.6 ± 1.1	Biogeochemical Model	Manizza et al. (2019)
	1996-2007		−0.5 ± 0.2	Biogeochemical Model	Manizza et al. (2013)
Chukchi Sea	1994-2019	-4.1±1.2	-12.1±3.6	Observation	This study
	1994-2019	-4.3±2.6	-14.4±8.6	Box-model	This study
			-9.2±1.9	Biogeochemical Model	Zheng et al., (2021b)
	1998-2015	-3.7±3.9			
	2006-2013	-3.0±0.6	-13.3±2.5	Biogeochemical Model	Manizza et al. (2019)
	1997-2014	-5.0±3.0		SOM technique	Yasunaka et al. (2018)
	1997-2013	-4.0±4.0		SOM technique	Yasunaka et al. (2016)
	2003-2014	-3.5 ± 2.0		Observation	Evans et al. (2015)
	1996-2007		-2.3±0.6	Biogeochemical Model	Manizza et al. (2013)
	1998-2003		-9.0±1.1	Multiple linear regression with remote sensing data	Arrigo et al. (2010)
	2002-2004	−14.0 ± 2.0	-46.0 ± 6.0	Observation	Bates et al. (2006)
	1998-2000	-12.0	-11.0	Observation	Murata and Takizawa (2003)
Western Arctic Ocean	1994-2019		-18.4±5.5	Observation	This study
	1994-2019		-22.5±13.8	Box-model	This study
	2006-2013		-17.6±5.0	Biogeochemical Model	Manizza et al. (2019)
	2003-2014		-10.9 ± 5.7	Observation	Evans et al. (2015)
	1998-2003		-18.6±3.3	Multiple linear regression with remote sensing data	Arrigo et al. (2010)
	1998-2004		-19.0 to -74.9	Integration of many studies	Bates and Mathis (2009)

*included the both the Beaufort Sea and Canada Basin.

Table 3. Correlation coefficients (r) between monthly CO_2 sinks and the associated variables. All correlation coefficients given here are statistically significant ($p<0.05$); a hyphen (-) indicates non-significant correlation.

	Beaufort Sea		Canada Basin		Chukchi Sea	
	Obs-based[a]	Modeled	Obs-based[a]	Modeled	Obs-based[a]	Modeled
Ice%	0.74	0.86	0.72	0.87	0.88	0.92
Second moment of wind speed	-0.11	-0.22	-	-0.40	-	-
Modeled ΔpCO_2	0.55	0.69	0.31	0.44	0.70	0.74
Modeled CO_2 flux	0.75	1.00	0.72	1.00	0.91	1.00

[a] CO_2 sink was estimated using the modified approach described in this study.